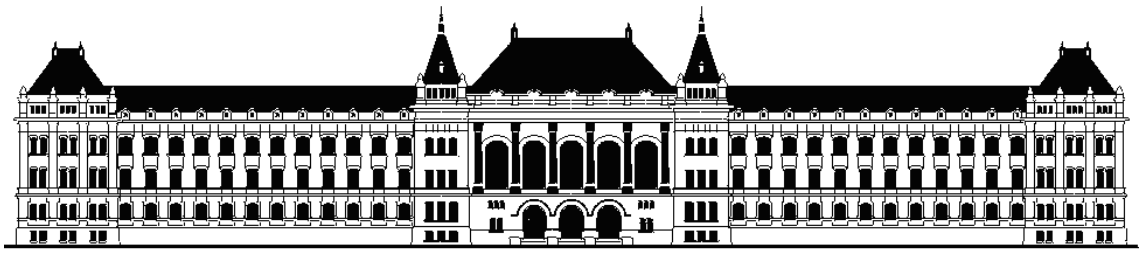

M Ű E G Y E T E M 1 7 8 2

Master's Thesis

Implementation and Analysis of Coil Compression Methods for Parallel Magnetic Resonance Imaging

István Homolya

Supervisor József Sinkó, PhD
MR Physicist
Mediso Kft.

Consultant Dávid Légrády, PhD
Associate Professor
Department of Nuclear Techniques
Institute of Nuclear Techniques

Budapest University of Technology and Economics

2019

FELADATKIÍRÁS

Az MR képalkotás gyorsítására szolgáló, szeleten belüli illetve egyszerre többszeletes Parallel Imaging módszerek alapötlete, hogy a hiányzó adatokat több, eltérő térbeli érzékenységi profilú mérőtekercs egyidejű használatával, azok mért adatainak kombinálásával pótoljuk. Különösen a kutatási célú, illetve a dinamikus mérések esetében a minél gyorsabb adatgyűjtésre való igény speciálisan a gyorsításra tervezett, nagy elemszámú (akár 64 elemből álló) mérőtekercsek piaci megjelenéséhez és elterjedéséhez vezetett. A mérőcsatornák egyre nagyobb száma ugyanakkor a rekonstrukció számításigényét rendkívüli módon megnöveli, ami – különösen az fMRI vizsgálatok esetében – az egyes mérések között szünetek beiktatását követelheti meg a rekonstrukció végeztéig, illetve szélsőséges esetben a valós idejű rekonstrukciót végző számítógép összeomlásához vezethet. A technikai problémákon kívül ez különösen nagy gondot okozhat az azonnali rekonstrukciót igénylő módszek, mint pl. a neurofeedback kísérletek esetén, amikor a kísérleti személynek a mérési adatokat majdnem-valós időben szeretnénk visszajelezni.

A nemrég publikált, ún. tekercs tömörítési (Coil Compression) eljárások segítségével lehetőség van a csatornaszám drasztikus csökkentésére, kihasználva, hogy az egyes tekercsek érzékenységi profiljai nem ortogonálisak, illetve az általuk kifeszített tér alacsonyabb dimenziós lehet, mint a tekercsek száma. Ennek köszönhetően lehetőség van kevesebb számú, virtuális tekercs matematikai létrehozására, oly módon, hogy a párhuzamos képalkotásra való képesség továbbra is megmarad, a képminőség romlása pedig minimális; a rekonstrukciós idő azonban jelentősen lecsökken.

A hallgató feladata a Coil Compression eljárások (főkomponens-analízis, vagy kiolvasó irányú geometriai tömörítés) matematikai hátterének megismerése, valamint a csökkentett tekercselem-szám hatásának vizsgálata a zajnövekedésre, illetve a műtermékek megjelenésére.

HALLGATÓI NYILATKOZAT

Alulírott *Homolya István* a Budapesti Műszaki és Gazdaságtudományi Egyetem fizika MSc szakos hallgatója kijelentem, hogy ezt a szakdolgozatot meg nem engedett segédeszközök nélkül, önállóan, a témavezető irányításával készítettem, és csak a megadott forrásokat használtam fel. Minden olyan részt, melyet szó szerint, vagy azonos értelemben, de átfogalmazva más forrásból vettem, a forrás megadásával jelöltem.

Budapest, 2019. május 18.

Homolya István

Acknowledgment

First and foremost, I would like to express my gratitude to Ádám Kettinger who inspired me to take the first steps on the long path of becoming an MR physicist. His expertise, dedication and enthusiasm showed the way in numerous cases. Without his help this thesis would have never been accomplished.

I am thankful for Dávid Légrády and Ferenc Simon who provided me precious opportunities in the field of MRI and opened new horizons throughout my Master formation. Their guidance has been extremely valuable.

I would like to thank my colleagues, especially Eszter Somogyi, Annamária Manga and Petra Hermann for making valuable comments and remarks on my work and actively participating in the in-vivo measurements. Furthermore, I am thankful for Zoltán Vidnyánszky who granted me access to the Magnetom Prisma medical scanner installed at Brain Imaging Center, Research Center for Natural Sciences, Hungarian Academy of Sciences.

Last but not least, I am very grateful to my family and partner for providing me a stable background in my personal life and supporting me for long years.

Contents

List of Symbols and Abbreviations

Symbols

Name	Symbol
intrinsic momentum/ spin	$\mathbf{S}$
magnetic moment	$\boldsymbol{\mu}$
gyromagnetic ratio	γ
external field	$\mathbf{B}_0$
torque	$\mathbf{N}$
Larmor-frequency	$\boldsymbol{\omega}_L$
macroscopic magnetization	$\mathbf{M}$
longitudinal relaxation time	T_1
transverse relaxation time	T_2
spatial coordinate	$\mathbf{r}$
k-space coordinate	$\mathbf{k}$
gradient strength	G_z
effective spin density	ρ
vector potential	$\mathbf{A}$
current density	$\mathbf{j}$
magnetic flux	Φ
coil sensitivity profile	$\mathcal{B}^{receive}$
raw k-space signal	S
image-space signal	I
superimposed sensitivity matrix	C
kernel of weights in k-space	w
kernel of weights in image-space	W
g-factor	g
acceleration factor	R
noise covariance matrix of set of coils	$\mathbf{\Psi}$
coil compression matrix	$\mathbf{A}$
complex conjugate operation	$*$
adjoint operation	$\dagger$
Fourier transform operation	$\mathcal{F}(\cdot)$
convolution operation	$*$
Nabla operator	∇
vector product	$\times$

Abbreviations

Name	Abbreviation
radio frequency	RF
electromotive force	*emf*
signal-to-noise ratio	SNR
Magnetic Resonance Imaging	MRI
Parallel Imaging	PI
Parallel Magnetic Resonance Imaging	pMRI
field of view	FOV
phase encoding	PE
readout	RO
Sensitivity Encoding	SENSE
Generalized Autocalibrating Partially Parallel Acquisition	GRAPPA
Autocalibration Signal	ACS
Coil Compression	CC
Principle Component Analysis	PCA
Optimized Transformation	OPT
Geometric-decomposition Coil Compression	GCC
independently identically distributed	IID

Chapter 1

Introduction

One of the most promising and most dynamically improving medical imaging modality of recent years has been Magnetic Resonance Imaging (MRI). Not only does it operate with non-ionizing radiation but MRI has also further considerable advantages compared to other medical imaging modalities. Application of different pulse sequences allows creating medical images with various contrast, thus a huge variety of anatomical and functional information can be extracted utilizing the same device.

However, one of the main drawbacks of this multipurpose tool is the lengthy acquisition. Total scan time of a high resolution anatomical scan can last up to 10 minutes, while the measurement of several images with different contrast, widely used in radiology, can endure 30 minutes. This can lead to a fall in possible applications both in clinical practice and research activity. In clinical diagnostics, not only may lengthy data acquisition decrease patient comfort but also increase the possibility of image artifacts, which is utmost undesirable. In addition, e.g. a computed tomography (CT) measurement, with a comparable spatial contrast and diagnostic value, can be performed in a fraction of a second.

In the hope of eliminating this problem, a significant percentage of MRI research and development has been intending to reduce total scan time while image quality remains untouched. Several endeavors were introduced in the late 1990's and early 2000's but only few of them achieved great success. The first breakthrough dates 1999, when Pruessmann et al. [12] presented the first clinically applicable Parallel Imaging (PI) technique, called Sensitivity Encoding (SENSE). Later on, Griswold et al. [13] introduced Generalized Autocalibrating Partially Parallel Acquisitions (GRAPPA). During the blossom of such early attempts was born the term Parallel Imaging (PI) referring to the common physical background of these techniques. All PI methods aim to reduce total scan time by acquiring less data than required for a conventional reconstruction method. In every case, the missing data is synthesized to recreate the total k-space. The mean of missing k-space data synthesis alters method by method, however they all exploit *implicitly* or *explicitly* the spatially

varying sensitivity profiles of receiver coils. Reconstruction algorithms adopt the additional information provided by the spatial variance of sensitivity profiles, which serve as a supplementary degree of freedom. Thus, the partially measured k-space can be completed numerically and the full image can be reconstructed.

As a result, a tendency for increased number of receiver coils in MRI measurements has emerged. Increased number of receiver coils offer several advantages such as increased SNR, more complete detection coverage of the sample and possible implementation of PI techniques.

On the other hand, increased number of receiver coils challenge scanner manufacturers to boost reconstruction hardware performance as reconstruction algorithms must run on all raw data of every receiver channel. Not only are procurement and maintenance of such powerful systems costly but the gain of shortened acquisition is lost at time-consuming reconstruction.

This thesis aims to investigate Coil Compression (CC) methods for PI which can reduce the amount of data sent to reconstruction hardware, as CC is performed right after acquisition prior to reconstruction. Consequently, time loss can be minimized.

In the first chapter of this thesis, a brief overview of Magnetic Resonance Imaging is given. Afterwards, clinically relevant Parallel Imaging techniques are presented. Noise amplification generated by the specific Parallel Imaging reconstruction is quantified and analytically derived. In the following chapters, the Coil Compression concept is introduced, followed by its effects on reconstruction amplified noise and image quality. Simulation and in-vivo measurement results are displayed.

Chapter 2

Fundamental Physics of Magnetic Resonance Imaging

2.1 Magnetic Resonance

Magnetic Resonance Imaging (MRI) is based on the phenomenon of magnetic resonance of the atomic nucleus, which reveals the origin of its former name, Nuclear Magnetic Resonance Imaging (NMRI). Every elementary particle possesses an intrinsic momentum ($\mathbf{S}$) [1], often referred to as *spin*. A magnetic moment ($\boldsymbol{\mu}$) can be associated with the spin of elementary particles [1]), defined as follows

$$\boldsymbol{\mu} = \gamma \mathbf{S} \tag{2.1}$$

where γ is a constant called gyromagnetic ratio. Gyromagnetic ratio is a unique constant for each elementary particle and/or nucleus, that is typically determined experimentally. As magnetic moment and spin only differs in a constant value, the two terms are used interchangeably throughout this thesis. Adequate discussion of MRI physics does not require quantum mechanical representation as the mean value of results derived using quantum mechanical representation is equal to the classical results [3]. Hence, from this time forth, problems are discussed in the classical picture.

Consider a static, uniform, external magnetic field $\mathbf{B}_0$ parallel to the z-axis of the coordinate system (Equation 2.2) and a magnetic moment $\boldsymbol{\mu}$ with an arbitrary angle with respect to the z-axis.

$$\mathbf{B}_0 = B_0 \mathbf{e}_z \tag{2.2}$$

The magnetic moment $\boldsymbol{\mu}$ experiences a torque $\mathbf{N}$, whose absolute value is proportional to the external field and its direction is perpendicular to the external field

and the magnetic moment at all times [1]. Mathematically, the torque is given by

$$\mathbf{N} = \boldsymbol{\mu} \times \mathbf{B}_0 \tag{2.3}$$

The torque can be expressed as the time derivative of the angular momentum [2], which in the current case yields

$$\mathbf{N} = \frac{\mathrm{d}\mathbf{S}}{\mathrm{d}t} = \frac{1}{\gamma}\frac{\mathrm{d}\boldsymbol{\mu}}{\mathrm{d}t} \tag{2.4}$$

Setting Equation 2.3 and 2.4 equal to each other, we obtain Bloch-equations (Equation 2.5) [4], which is the equation of motion of such a magnetic moment in an external magnetic field.

$$\frac{\mathrm{d}\boldsymbol{\mu}}{\mathrm{d}t} = \gamma\boldsymbol{\mu} \times \mathbf{B}_0 \tag{2.5}$$

The presence of the external field forces the magnetic moment to precess around the external field, i.e. the z-axis in the current setup. The equation of motion is analogous to the one of a spinning gyroscope. Herein lies the explanation for the terms 'spin' and 'gyromagnetic ratio'.

The angular frequency of the precession is given in Equation 2.6, where both the vectorial and scalar forms are indicated. The negative sign in the vectorial form indicates the negative, i.e. clockwise direction of the precession.

$$\boldsymbol{\omega}_L = -\gamma\mathbf{B}_0 \qquad \omega_L = \gamma B_0 \tag{2.6}$$

The precessing magnetic moments induce a changing magnetic field, which can be detected with coils placed around the sample. The MRI signal comes from the perpendicular component of the magnetic moments with respect to the z-axis as the parallel components with respect to the z-axis have no time dependence. This statement is valid only if relaxation is neglected. Magnetic moments reach their equilibrium when they are parallel to the external magnetic field. The transverse component becomes zero, the MRI signal disappears.

2.2 Rotating Reference Frame, Excitation and Relaxation

Excitation denotes the energy transfer into the precessing magnetic moments via radiofrequency (RF) pulse. RF pulse put the magnetic moments into a higher energy state from the ground state, hence they produce a net transverse magnetization. Precession and relaxation are simultaneously present until the spins return to the

ground state. As long as the net transverse magnetization is present, the radiated energy can be observed, which provides the MRI signal. In clinical practice (for human body tissue) the precession-induced magnetic field has six orders of magnitude greater amplitude than the relaxation-induced field [3]. Consequently, the latter term is generally neglected in MRI. However, in solid state NMR this statement no longer holds and both must be taken into account.

To discuss RF excitation, it is useful to make a transition from the laboratory reference frame into the rotating reference frame. Let ω' denote the angular frequency of the precession of the magnetic moments in the rotating frame, ω_L the Larmor-frequency in the laboratory reference frame and ω the angular frequency of the rotating reference frame. Thus, $\omega' = \omega_L - \omega$ holds all times. If the angular frequency of the rotating system matches the Larmor-frequency, then the magnetic moments seem to stand still in the rotating frame, that is $\omega' = \omega_L - \omega = 0$. This special framework can be handled as if the external magnetic field was zero, that is $\mathbf{B}_0 = \mathbf{0}$. In the upcoming paragraph the statement is proved.

Consider a rotating reference frame with arbitrary angular frequency $\mathbf{\Omega}$. Equation 2.7 holds for the time derivatives of an arbitrary vector $\mathbf{V}$ [2], where the time derivative with comma denotes the rotating frame, while the time derivative without comma denotes the laboratory frame. Hence, Equation 2.7 equally holds for Equation 2.8.

$$\frac{\mathrm{d}\mathbf{V}}{\mathrm{d}t} = \left(\frac{\mathrm{d}\mathbf{V}}{\mathrm{d}t}\right)' + \mathbf{\Omega} \times \boldsymbol{V} \tag{2.7}$$

$$\frac{\mathrm{d}\boldsymbol{\mu}}{\mathrm{d}t} = \left(\frac{\mathrm{d}\boldsymbol{\mu}}{\mathrm{d}t}\right)' + \mathbf{\Omega} \times \boldsymbol{\mu} \tag{2.8}$$

The time derivative of the magnetic moment is known in the laboratory frame (Equation 2.5). Setting Equation 2.8 and 2.5 equal, then using the properties of the vector product, we find Equation 2.13. The steps of the derivation are indicated below.

$$\gamma\boldsymbol{\mu} \times \boldsymbol{B} = \left(\frac{\mathrm{d}\boldsymbol{\mu}}{\mathrm{d}t}\right)' + \mathbf{\Omega} \times \boldsymbol{\mu} \tag{2.9}$$

$$\gamma\boldsymbol{\mu} \times \boldsymbol{B} = \left(\frac{\mathrm{d}\boldsymbol{\mu}}{\mathrm{d}t}\right)' - (\boldsymbol{\mu} \times \mathbf{\Omega}) \tag{2.10}$$

$$(\gamma\boldsymbol{\mu} \times \boldsymbol{B}) + (\boldsymbol{\mu} \times \mathbf{\Omega}) = \left(\frac{\mathrm{d}\boldsymbol{\mu}}{\mathrm{d}t}\right)' \tag{2.11}$$

$$\gamma\boldsymbol{\mu} \times \left(\boldsymbol{B} + \frac{\mathbf{\Omega}}{\gamma}\right) = \left(\frac{\mathrm{d}\boldsymbol{\mu}}{\mathrm{d}t}\right)' \tag{2.12}$$

$$\left(\frac{\mathrm{d}\boldsymbol{\mu}}{\mathrm{d}t}\right)' = \gamma\boldsymbol{\mu} \times \boldsymbol{B}_{eff} \qquad \boldsymbol{B}_{eff} = \boldsymbol{B} + \frac{\boldsymbol{\Omega}}{\gamma} \tag{2.13}$$

$$\boldsymbol{B}_{eff} = \boldsymbol{B} + \frac{\boldsymbol{\Omega}}{\gamma} = \boldsymbol{B} + \frac{(-\gamma\boldsymbol{B})}{\gamma} = 0 \tag{2.14}$$

Inserting the definition of Equation 2.6 into Equation 2.13, we find that the magnetic moments indeed seem to stand still in a reference frame rotating with the exact Larmor-frequency (Equation 2.14). This specific rotating frame seems a natural choice, and from this time forth, the magnetic moments are considered in this specific rotating frame.

Consider an additional magnetic field $\mathbf{B}_1$=$\mathrm{B}_{x'}\mathbf{e}_{x'}$ in the rotating reference frame[1]. The magnetic moments are excited from the equilibrium and are precessing in the y'-z' plane, whereas, in the laboratory frame, they follow a complicated trajectory as a superposition of two simultaneous precessions. As a result, the magnetic moments gain a transverse component, a detectable MRI signal is induced. The procedure is called excitation in the MRI literature, whereas the 'radiofrequency' prefix refers to the range of the Larmor-frequency of the $\mathbf{B}_1$ field. As MRI devices available in clinical practice operate with field of 1-3 T, the excitation is in the range of radiofrequency. RF excitation is commonly referred to as RF 'pulses' since their millisecond duration is considered a point-like time event compared to the rest of the acquisition [3]. RF pulses are characterized by the flip angle in degree or radian, such as 90° or $\pi/2$ pulse, 180° or π pulse, etc.

It is worth to take a moment to highlight the accuracy of the expression *resonance* in Magnetic Resonance Imaging. Magnetic moments are capable of absorbing energy only in a narrow range around the Larmor-frequency [5]. Quantum mechanical derivation of magnetic resonance proves that only a narrow range around $\omega = \omega_L$ of the induced emission and absorption spectrum shows a considerable peak [2]. Thus, a resonance frequency can be defined that can be treated analogous to the classical forced resonance [2]. Adopting the analogy to the classical picture, one can state that the requirement of perfect excitation is the matching Larmor-frequency for RF pulse $\mathbf{B}_1$.

Magnetization, i.e. the density of magnetic moments in a volume unit, is defined in Equation 2.15. Bloch-equations are still valid as the magnetization is the vectorial summation of single magnetic moments.

$$\mathbf{M} = \frac{1}{V}\sum_i \boldsymbol{\mu}_i \tag{2.15}$$

[1]In MRI literature the directions of the standing reference frame are denoted by the common x,y,z parameters, whereas the directions of the rotating frame are denoted by capital letters X,Y,Z or extra commas x',y',z'.

The relaxation of the magnetization is due to two simultaneous procedures; a longitudinal and a transverse relaxation. After an RF excitation the longitudinal magnetization decays according to Equation 2.16, which is characterized by the first-order time constant T_1. Equation 2.16 describes two concurrent processes; the longitudinal magnetization $M_z(0)$ built up by the RF pulse decays, while the initial magnetization $M_0(0)$ reaches its maximum.

$$M_z(t) = M_z(0)e^{-t/T_1} + M_0(1 - e^{-t/T_1}) \tag{2.16}$$

The transverse magnetization (component perpendicular to the external field) decays according to Equation 2.17.

$$M_{xy}(t) = M_{xy}(0)e^{-t/T_2} \tag{2.17}$$

Longitudinal and transverse relaxation truly differ in their nature. Longitudinal relaxation includes interaction and energy transfer to the environment, whereas transverse relaxation occurs due to temporary statistical phase decoherence [3]. Typical values of T_1 and T_2 vary according to materials and cover a huge range from a few nanoseconds until a few seconds. In practice, $T_2 \leqslant T_1$ generally holds. It is noteworthy that none of these relaxation are recoverable, true information loss occurs.

2.3 One Dimensional Imaging

Basic concept of Magnetic Resonance Imaging can be introduced via one dimensional imaging. Notions, quantities are defined in one dimension that are later generalized for higher dimensions. During current discussion, relaxation is neglected and a one dimensional effective spin density along z-axis is considered.

MRI highly relies on the direct relation between the Larmor-frequency of spins and the strength of the external magnetic field, as discussed in Section 2.1. If there is a given spatial dependence of the external field $\mathbf{B}_0$, consequently a spatial dependence of the Larmor-frequency appears. The relation can be exploited as follows: signal, originated from a spin, carries information on the spatial location on the given spin if the magnetic field has a spatial dependence. Consider the following spatial dependence of the external field, denoted by Equation 2.18 and 2.19. After a simple insertion, Larmor-frequency of the spins can be written as in Equation 2.20. Spatial derivative in Equation 2.19 is called *gradient strength*, whereas the spatially dependent external magnetic field $G_z \cdot z$ is referred to as *gradient field*.

$$B(z) = B_0 + G_z \cdot z \tag{2.18}$$

$$G_z = \frac{\partial B(z)}{\partial z} \tag{2.19}$$

$$\omega_L = \gamma B_z = \gamma B_0 + \gamma G_z \cdot z \tag{2.20}$$

To put it in another way, if the spectral distribution of the MRI signal is known, then, after a simple rescaling, the contribution to the signal of a given spin at a specific coordinate z can be calculated. The mathematical tool for acquiring spectral distribution is known as Fourier transform [6]. In a nutshell, once a linear gradient field is activated, the inverse Fourier transform of the time dependent signal returns the one dimensional image of the spin density along the z-axis. Mind that a linear gradient field is essential to maintain the linear features of imaging and to minimize image distortion by virtue of higher terms of the non-linear gradient field.

2.4 k-space and Resolution in One Dimensional Imaging

MRI signal disappears typically 1 ms after a gradient field is switched on. Quantitative description of gradient fields require new terminology, which was created by the introduction of *k-space*.

Switching on gradient fields can be interpreted as the intentional augmentation of external field inhomogeneity, which leads to an extremely quick spin decoherence. The effect of gradient fields bears a strong resemblance of the spin decoherence experienced when performing a Free Induction Decay (FID) experiment [3]. Just as it is possible to recover the signal loss by reversing T_2^* decay in a standard NMR spin echo experiment [3], signal loss due to gradient fields can be reversed by switching on another external gradient field with opposite polarity. Consider a spin population in a constant, spatially non-varying phase. Now turn on a positive gradient field. Those spins who experience a greater external field than in the ground state accumulate positive phase with respect to a reference spin that is located in the origin. Once the other gradient field with the opposite polarity is put on, the same spins experience a smaller field, their relative phase decreases. If the gradient field with the opposite polarity is on long enough, all spins lose their accumulated relative phase, and all spins have the same phase, hence a detectable MRI signal is recovered. This phenomenon is called *gradient echo*.

The aforementioned relative phase can be defined as follows

$$\phi(z,t) = \gamma z \int_0^t G_z(t')\mathrm{d}t' \tag{2.21}$$

Let us define a new quantity k_z as follows

$$k_z(t) := \frac{\gamma}{2\pi} \int_0^t G_z(t')\mathrm{d}t' \tag{2.22}$$

Equation 2.23 holds for a typical MRI acquisition, that is, the integral of the complex-valued effective spin density (ρ) is measured during an MRI scan.

$$S \propto \int \rho(z) e^{-i\phi(z,t)} \mathrm{d}z \tag{2.23}$$

Adopting Equation 2.22 into Equation 2.23, we find

$$S \propto \int \rho(z) e^{-i2\pi k_z \cdot z} \mathrm{d}z = S(k_z) = F\{\rho(z)\} \tag{2.24}$$

It has been proved that, if the relative phase is due to a linear external gradients field, the MRI signal is proportional to the Fourier transform of the effective spin density. As a result of the Fourier transform, the natural variable of the signal becomes k_z. Two quantities, z and k_z are alluded to as Fourier conjugate variables, since k_z bears the same dependence on z as the frequency f bears on time t, variables commonly used in conventional Fourier transform.

Analyzing Equation 2.22, one can realize that the highest detectable spatial frequency, which is described by Equation 2.24, is proportional to the time integral of the gradient field. If the gradient field is constant in time, then it is proportional to the acquisition time. This criteria is the special case of the Nyquist-Shanon sampling theorem [8]. The longer a time dependent signal is sampled, the higher the resolution of the spectrum is, that is, the higher the spatial resolution is, translating the Nyquist-Shannon sampling theorem to the very special case of MRI.

Consequences of fast spin decoherence are to be kept in mind when measurement techniques and protocols are designed. Signal amplitude of high k values are small due to the accumulated relative spin phase. Consequently, low k values contain most of the relevant information. An optimal signal acquisition protocol can be set up if the herein discussed gradient echo sequence is applied. Signal acquisition is launched at the exact same moment when a negative gradient field is switched on, after a positive gradient field has been applied. This methods reorganizes spin coherence, i.e. takes them back to k=0, while positive and negative k values are equally covered.

2.5 Two Dimensional Imaging and Field-of-View

During a conventional two dimensional scan, data is collected around k=0 in a rectangular lattice. Image is gained via a simple 2D Fourier transform. The simplest way to cover the rectangular formed region-of-interest (ROI) in k-space, is the sys-

tematical repetition of the aforementioned 1D gradient echo sequence. Signal loss due to T_2^* decay is not reversed by the 2D gradient echo, which is one of its major drawbacks [3]. To overcome this fault, has been introduced the *spin echo* sequence [3]. Argumentation on the accumulated relative spin phase and on signal acquisition concepts, that has previously been derived for gradient echo, still holds for spin echo. However, the major difference between a gradient echo and a spin echo sequence lies in the way of provoking spin phase recovery. While the accumulated relative phase is annulled by switching gradient polarity at a gradient echo sequence, spin echo sequences achieve this with an extra 180° pulse. Thus, gradient polarity does not need to be reversed during the acquisition. Application of a 180° pulse can be interpreted as time-reversing [3], which gives the explanation on why T_2^* decay can be reversed. As T_2^* decay is caused by $\mathbf{B}_0$ field inhomogenity, a simple inversion acts as if the $\mathbf{B}_0$ field had been inverted, which recovers phase accumulation.

During a 2D spin/gradient echo sequence, two gradient fields are activated: one is switched on during the acquisition, which is referred to as *readout* (RO) or *frequency-encoding* gradient in MRI nomenclature, the other tunes the relative phase of the spins before acquisition. The latter is called *phase-encoding* (PE) gradient. A comparative figure of the conventional spin ans gradient echo is displayed in Figure 2.1, utilizing the usual nomenclature.

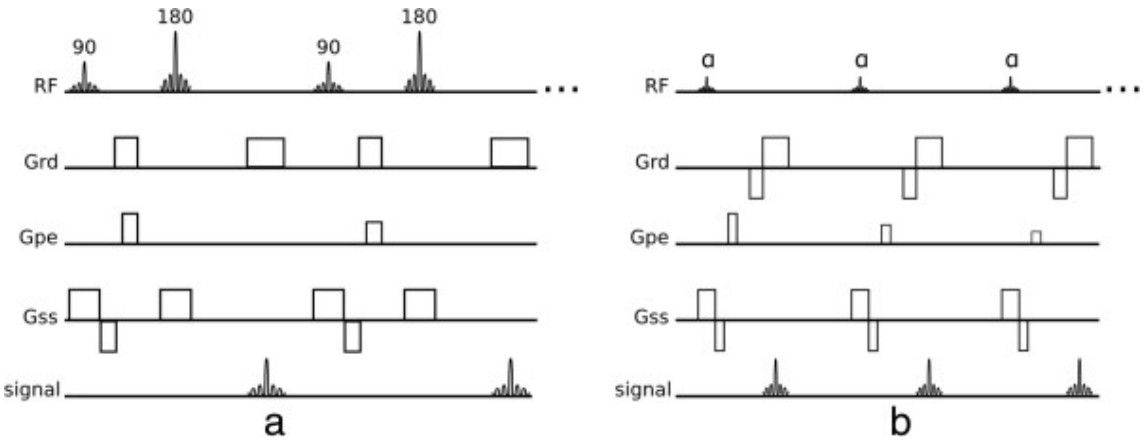

Figure 2.1: [9] Sequence diagram of a conventional spin echo (a) vs. gradient echo (b). Both sequences are repeated several times. Readout gradients (G_{rd}), phase-encoding (G_{pe}) and slice selecting gradients (G_{ss}) are denoted, as well as RF pulses and data acquisition (signal). The major difference between a conventional spin echo vs. gradient echo lies in the number of RF pulses (90° & 180° vs. 90°, respectively) and the readout gradient polarity (one polarity vs. reversed polarity, respectively). On the sequence diagram of the gradient echo (a), α denotes an arbitrary flip angle for the RF excitation.

As MRI is a digital device, data sampling is performed in every Δt step. It is a valid assumption that RO direction is sampled continuously, while PE direction is covered in discrete steps. Discrete PE sampling leads to the definition of the

field-of-view (FOV). FOV is the region which imaging can provide information of. It is essential to have a large enough FOV that includes the ROI in all sampling directions, especially in the PE direction, to avoid image artifacts. In case of a small FOV, the outlying regions are not simply cut off from the final image, but they appear on the opposite site, i.e. *wrapping-around* or *aliasing*.

Wrapping-around is a direct consequence of Nyquist-Shannon sampling theorem [8]. If the time dependent signal is not sampled fast enough, i.e. PE steps are too large, high frequency components are cut off from the frequency spectrum, and wrap around the low frequencies, resulting in aliasing.

2.6 Slice Selection and Three Dimensional Imaging

In clinical practice, 2D scans have gained popularity over 3D scans due to their time-economic features. During a 2D scan, the effective spin density in the third direction is integrated, that is a projected image is produced. However, the distortion of the projection can be decreased by *slice selection*. Slice selection prevents a complete projection along the third axis, and only integrates the signal in the interval defined by the slice selection. Covering the third direction with equidistant 2D scans, the whole set of images provides sufficient amount of medical information. It is essential to chose a slice thickness wisely, not to integrate over a region where major anatomical changes occur in human body.

Slice selection is performed by the activation of a gradient field during RF excitation (as displayed on Figure 2.1). Direct dependency of the Larmor-frequency on the external field is the key element for slice selection. The bandwidth of the RF pulse defines the slice width which spins are excited in, as their Larmor-frequency is in same bandwidth as the frequency of the RF pulse. Bear in mind that the excited slice is perpendicular to the applied slice selection gradient field.

2.7 The MRI Signal and the Principle of Reciprocity

In the previous paragraphs, the central topic has been to describe the changes in the magnetic field of a sample by virtue of the presence of an external magnetic field. It has been shown that, once the magnetization has gained a transverse component, the detection of the precession can be considered.

MRI signal detection is performed via coils that are placed around the sample. The sample's own magnetic field varies over time due to precession, hence an electromotive force (emf) is induced in the surrounding coil, a consequence of Faraday's law of induction [24]. The emf, that is, the detected MRI signal S, induced in the coil can be written as follows

$$emf = S = -\frac{\mathrm{d}\Phi}{\mathrm{dt}} \tag{2.25}$$

where Φ denotes the flux of the precessing spins sweeping through the coil surface. Definition of magnetic flux can be reformulated utilizing Stoke's theorem [25] as follows

$$\Phi = \iint_S \mathbf{B}\mathrm{d}\mathbf{S} = \oint_l \mathbf{A}\mathrm{dl} \tag{2.26}$$

where $\mathbf{B}$ denotes the magnetic field, $\mathbf{A}$ stands for the vector potential. Let us suppose quasi-static approximation of magnetic fields, which allows neglecting radiation terms. The approximation holds for small magnetic fields [26]. As a result, the vector potential yields

$$\mathbf{A}(\mathbf{r}) = \frac{\mu_0}{4\pi}\int \mathrm{d}^3\mathbf{r}'\frac{\mathbf{j}(\mathbf{r}')}{|\mathbf{r}-\mathbf{r}'|} \tag{2.27}$$

Current density $\mathbf{j}(\mathbf{r}')$ of the sample is associated with the magnetic field of the sample.

$$\mathbf{j}(\mathbf{r}') = \nabla \times \mathbf{M}(\mathbf{r}') \tag{2.28}$$

Plugging Equation 2.28 into Equation 2.27 and 2.26, we find

$$\begin{aligned}
\Phi = \oint_l \mathbf{A}\mathrm{dl} &= \oint_l \mathrm{dl}\left[\frac{\mu_0}{4\pi}\int \mathrm{d}^3\mathbf{r}'\frac{\mathbf{j}(\mathbf{r}')}{|\mathbf{r}-\mathbf{r}'|}\right] \\
&= \oint_l \mathrm{dl}\left[\frac{\mu_0}{4\pi}\int \mathrm{d}^3\mathbf{r}'\frac{\nabla'\times\mathbf{M}(\mathbf{r}')}{|\mathbf{r}-\mathbf{r}'|}\right] \\
&= \frac{\mu_0}{4\pi}\int \mathrm{dl}\int \mathrm{d}^3\mathbf{r}'\left[\frac{-\nabla'}{|\mathbf{r}-\mathbf{r}'|}\times\mathbf{M}(\mathbf{r}')\right] \\
&= \frac{\mu_0}{4\pi}\int \mathrm{d}^3\mathbf{r}'\mathbf{M}(\mathbf{r}')\left[\nabla'\times\left(\oint\frac{\mathrm{dl}}{|\mathbf{r}-\mathbf{r}'|}\right)\right]
\end{aligned} \tag{2.29}$$

The specific case of Equation 2.27 for current loops shows that the curl of the line integral over the current path in Equation 2.29 is actually the magnetic field per unit current that would be produced by the coil at the point $\mathbf{r}'$ [3]. The quantity $\mathcal{B}(\mathbf{r}')^{receive}$, boarded by rectangular parenthesis in Equation 2.29, is referred to as *coil sensitivity profile*, which is widely used to characterize coils.

$$\mathcal{B}^{receive} = \mathbf{B}/I = \nabla'\times\left(\frac{\mu_0}{4\pi}\oint\frac{\mathrm{dl}}{|\mathbf{r}-\mathbf{r}'|}\right) \tag{2.30}$$

Flux (Equation 2.29) can be rewritten as

$$\Phi = \int \mathrm{d}^3\mathbf{r}' \mathcal{B}(\mathbf{r}')^{receive} \mathbf{M}(\mathbf{r}', \mathbf{t}) \tag{2.31}$$

Equation 2.31 declares the *principle of reciprocity*, i.e. the flux depends on the receive field, that is produced by current induced by the change of flux in the receiver coil [3]. Higher the induced voltage is as a response of the change of magnetization, the more sensible the coil is. Coil sensitivity profiles serve as spatial weighting of signal, which highly affects signal detection. Signal contribution of spins situated farther from the coil center are suppressed, whereas the signal of closely located spins are relatively magnified.

Coil sensitivity profiles vary over design, dimension and manufacturer. However, purpose of the coil largely defines the possible coil sensitivity configuration. Transmitter body coils possess homogeneous sensitivity profiles over a wide region, whereas local receiver surface coils own sensitivity maps that vary intensively in space. In the upcoming chapters, weighting of the spatially varying sensitivity maps are used to introduce modern and robust techniques for total acquisition time reduction.

Chapter 3

Parallel Magnetic Resonance Imaging

This chapter contains an in-depth discussion of the PI techniques which benefit from the spatially varying coil sensitivity profiles. The techniques presented here are in-plane acceleration methods. Thus, the conventional MRI terminology regarding 2D scans is commonly used.

3.1 Image-space reconstruction: SENSE

Consider an ideal MRI experiment scenario with a single receiver channel possessing a homogeneous sensitivity profile. The raw measured signal is proportional to the simple Fourier transform of the effective spin density $\rho(\mathbf{r})$, as denoted below

$$S(t) \propto \int \rho(\mathbf{r}) e^{-i2\pi \mathbf{kr}} \mathrm{d}^3\mathbf{r} \tag{3.1}$$

However, when dealing with numerous, non-ideal receiver channels, there is another practical aspect to consider, namely the spatially varying sensitivity profiles, as described in Section 2.7. Consider a coil with N receiver channels where $\mathcal{B}(\mathbf{r}')_j^{receive}$ designates the sensitivity profile of the j-th channel. The signal of the j-th channel can be expressed as follows

$$S_j(t) \propto \int \rho(\mathbf{r}) \mathcal{B}(\mathbf{r})_j^{receive} e^{-i2\pi \mathbf{kr}} \mathrm{d}^3\mathbf{r} \tag{3.2}$$

The effective spin density is voxel-wisely multiplied by the sensitivity profile of the given channel. Consequently, the raw signal is weighted by the receiver channel's very own sensitivity profile $\mathcal{B}(\mathbf{r})_j^{receive}$, thus, additional information is encoded into the signal, which can be put to use.

PI techniques aim to realize some serious time gain by accelerating the measurement by undersampling k-space. The concept behind SENSE is to increase the equidistant k-space steps in PE direction (Figure 3.1), i.e. decreasing the FOV in PE direction, thus accelerating the data acquisition. Missing k-space data is synthesized by the *explicit* use of sensitivity profiles. Spatial resolution does not change as the extent of k-space coverage remains untouched, i.e. k-space is still equidistantly sampled from $-k_{max}$ to k_{max}. However, during acquisition, only a fraction of the original k-space is covered as the distance between successive k-space lines has increased. In MRI literature the systematic undersampling ratio of k-space in the PE direction is known as *acceleration factor* (R). RO direction is fully sampled, no acceleration is applied in that direction, compared to a conventional scan.

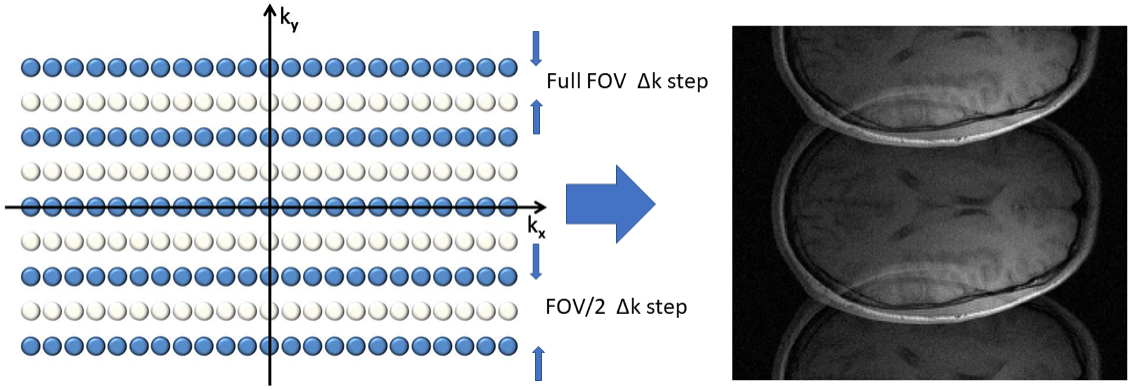

Figure 3.1: Effect of decreased FOV on image quality. On the left: k-space steps for a large enough FOV and k-space steps for FOV/2 case are denoted, respectively. Blue and white dots denote measured data and unmeasured data, respectively. k_x and k_y stand for the RO and PE direction, respectively. Displayed example represents k-space steps of an acceleration factor of 2. On the right: wrap-around artifact in the PE direction due to small FOV.

The gain in total scan time is proportional to the acceleration factor. However, performing a conventional inverse Fourier transform on such dataset would result in aliasing in the PE direction which is utmost objectionable. To avoid such artifact, the missing k-space lines in PE direction are synthesized utilizing the sensitivity maps. This implies that SENSE reconstruction algorithm requires two datasets: the measurement of coil sensitivity maps and the accelerated measurement.

Consider the simplest SENSE measurement scenario with receiver coils $N = 2$ and acceleration factor $R = 2$. Let I_1 and I_2 denote two voxels of the image-space signal, i.e. two voxels achieved after the simple inverse Fourier transform of raw k-space signal S_1 and S_2 ($I = \mathcal{F}^{-1}(S)$). It should be noted that image-space signal I suffers from aliasing and the degree of aliasing is encoded by R. Hence, the term *superimposed voxel* or *overlapping voxel* can be introduced to denote a voxel containing information from R separate coordinates of the effective spin density.

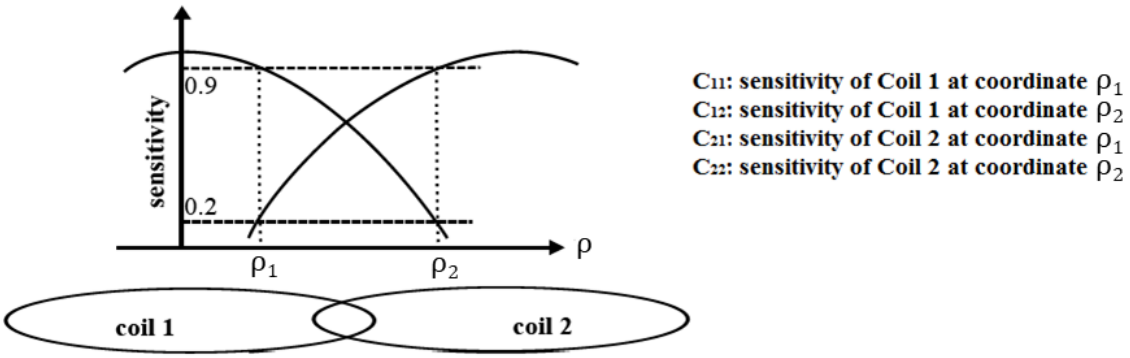

Figure 3.2: [3] Schematic figure of signal weighting. Spatially varying coil sensitivity profiles weight the one dimensional effective spin density (ρ) according to their spatial position. Weighting enables voxel separation, thus regaining separate signals of overlapping voxels.

I_1 and I_2 belong to coordinates x_1 and x_2, where the effective spin density is ρ_1 and ρ_2, respectively. Voxel distance yields $\Delta x = |x_2 - x_1| = \frac{FOV_{PE}}{2}$. Voxel distance Δx is not an arbitrary value, but is *implicitly* encoded by the aliasing via the acceleration factor, that is, in general, $\Delta x = \frac{FOV_{PE}}{R}$. Let C_{ij} stand for the value of the sensitivity profile of the i-th channel at coordinate x_j. A schematic demonstration of sensitivity profile is displayed on Figure 3.2. The image-space signal of the two superimposed voxels can be written as follows

$$I_1 = C_{11}\rho_1 + C_{12}\rho_2 \qquad I_2 = C_{21}\rho_1 + C_{22}\rho_2 \tag{3.3}$$

Using the more suitable vector and matrix formalism, Equation 3.3 can be reformulated as follows

$$\begin{bmatrix} I_1 \\ I_2 \end{bmatrix} = \begin{bmatrix} C_{11} & C_{12} \\ C_{21} & C_{22} \end{bmatrix} \begin{bmatrix} \rho_1 \\ \rho_2 \end{bmatrix} \tag{3.4}$$

Reformulation offers a great possibility to make a full transition into the generalized discussion of the problem with arbitrary receiver channels N and acceleration factor R.

$$\mathbf{I} = \begin{bmatrix} I_1 \\ I_2 \\ \vdots \\ I_N \end{bmatrix} \quad \mathbf{C} = \begin{bmatrix} C_{11} & C_{12} & \cdots & C_{1R} \\ C_{21} & C_{22} & \cdots & C_{2R} \\ \vdots & \vdots & \ddots & \vdots \\ C_{N1} & C_{N2} & \cdots & C_{NR} \end{bmatrix} \quad \boldsymbol{\rho} = \begin{bmatrix} \rho_1 \\ \rho_2 \\ \vdots \\ \rho_R \end{bmatrix} \tag{3.5}$$

Adopting Equation 3.5 in Equation 3.4 yields

$$\mathbf{I} = \mathbf{C}\boldsymbol{\rho} \tag{3.6}$$

It is important to note that, in general, the sensitivity matrix of superimposed voxels $\mathbf{C}$ is a non-square matrix. However, in order to get an overdetermined solution for $\boldsymbol{\rho}$, $\mathbf{C}$ must contain more rows than columns. As a result, a physical realization criteria can be set: the number of receiver channels must be greater than or equal to the acceleration factor ($N \geq R$). In general, an exact solution for $\boldsymbol{\rho}$ cannot be computed, but a fair enough approximation can be estimated using the Moore-Penrose pseudoinverse [19] of the sensitivity matrix.

$$\boldsymbol{\rho} = \mathbf{C_P^{-1}I} = (\mathbf{C^\dagger C})^{-1}\mathbf{C^\dagger I} \tag{3.7}$$

The Moore-Penrose pseudoinverse $\mathbf{C_P^{-1}}$ provides the most suitable solution based on the method of least squares known from regression analysis [19].

It has been shown that the *explicit* knowledge of coil sensitivity maps opens a new horizon in special reconstruction algorithms. However, extracting the accurate sensitivity map of a setup is not straightforward as they may differ from patient to patient due to electromagnetic coupling between the human body and the coil [12]. Thus, a typical SENSE protocol consists of a low resolution prescan of the sensitivity maps and the accelerated measurement with the desired user parameters. Furthermore, patient movement can seriously affect image quality as image reconstruction is largely based on prior knowledge of the sensitivity maps of the given measurement setup. If the setup parameters change, the accumulating phase errors will result in remaining aliasing artifacts on the final image.

So far the impact of noise on reconstruction has been neglected. The ordinary least squares method in Equation 3.7 is SNR optimal only if the measurement noise of each channel is independent of one another and has the same variance in all receiver channels. As this is usually not the case in practice, the noise covariance between receiver channels has to be taken into account. Detailed discussion of noise amplification by the reconstruction and how the noise covariance of coils should be taken into consideration in reconstruction is described in Section 3.3.1.

3.2 Reconstruction in k-space: GRAPPA

SENSE reconstruction is performed in image-space. However, the natural representation of raw MRI data is in k-space. Hence, the idea arose naturally: it would be fortunate to synthesize the missing k-space data in k-space, right before transitioning into image-space with a simple inverse Fourier transform. This concept lead to the rise of k-space-based algorithms which do not require the *explicit* knowledge of sensitivity maps. Several k-space-based techniques have been developed, but the most widespread is Generalized Autocalibrating Partially Parallel Acquisitions

(GRAPPA), first presented by Griswold et al. [13].

The accelerated measurement is executed exactly the same way as in the case of SENSE; k-space steps in PE direction are increased, i.e. decreasing the FOV in PE direction. The missing k-space lines, however, are right away synthesized in k-space. The concept is the following: the neighboring points of each missing k-space point contain some information on the missing points. This prior knowledge is used for data synthesis. Information blurring is originated from the convolution of the Fourier transform of the effective spin density and the Fourier transform of the sensitivity maps. Whereas, in case of SENSE, the spin density is weighted by the spatially varying sensitivity maps, i.e. voxel-wise product of the two quantities in image-space, in k-space, the Fourier transform of the two quantities are convoluted. The convolution in k-space is responsible for the information blurring. Equation 3.8 demonstrates the aforementioned equality and designates that inverse Fourier-transform to regain the image.

$$\underbrace{\mathcal{F}^{-1}(\mathcal{F}(\mathbf{I}\cdot\mathbf{C}))}_{SENSE} = \underbrace{\mathcal{F}^{-1}(\mathcal{F}(\mathbf{I})*\mathcal{F}(\mathbf{C}))}_{GRAPPA} \tag{3.8}$$

It is noteworthy that information blurring is only significant to the extent of the support of the Fourier transform of the coil sensitivity maps. This gives an intuition of the extent of the kernel size as no further gain belongs to a kernel whose size is considerable larger than the Fourier transform of the coil sensitivity maps.

Every missing k-space point is computed as the linear combination of the surrounding points, which mathematically can be reformulated as in Equation 3.9. $S_j(\mathbf{k}_l)$ denotes the missing data at k-space location $\mathbf{k}_l$ from the j-th coil, while $S_m(\mathbf{k}_n)$ stands for the measured data at k-space location $\mathbf{k}_n$ from the m-th coil. The k-space weights w bear all aforementioned indices; m denotes the source coil, n stands for the source data index, while j denotes the target coil, n stands for the target data index of $w_{j,l,m,n}$. The k-space set of weights $w_{j,l,m,n}$ is also referred to as *kernel* in MRI literature [14].

$$S_j(\mathbf{k}_l) = \sum_{m,n} w_{j,l,m,n} S_m(\mathbf{k}_n) \tag{3.9}$$

If equidistant sampling is respected, kernel derivation only requires the relative k-space coordinates $(l-n)$ (Equation 3.10), as the same kernel is swept through the k-space [14]. Kernel w is composed of N^2 subkernels as all data from source coils (N) are utilized to compute missing data for all target coils (N). Derivation of subkernels only requires the relative coordinates $(l-n)$, as the source and the target coils are used explicitly.

$$S_j(\mathbf{k}_l) = \sum_{m,n} w_{j,m,l-n} S_m(\mathbf{k}_n) \tag{3.10}$$

Ideal combination weights are derived from the autocalibration signal (ACS) dataset. The calibration kernel is swept through the ACS dataset and at each k-space location a source and a target vector is built, as displayed in Figure 3.3. Once covering the whole ACS k-space, all source and target vectors are concatenated horizontally, yielding the source ($\mathbf{S}_{source}$) and target matrices ($\mathbf{S}_{target}$). Information blurring ensures the connection between the source and target matrices, which is established by the combination weights in Equation 3.11. Combinations weights are derived by inverting Equation 3.11 using the Moore-Penrose pseudoinverse, which results in Equation 3.12. Finally, the same kernel is swept through on the k-space of the accelerated measurement, but this time only building the source matrix. Inserting the derived combination weights $\mathbf{w}$ and the newly formed source matrix $\mathbf{S}_{\mathbf{source}}$ into Equation 3.11, the target matrix $\mathbf{S}_{target}$ can be computed.

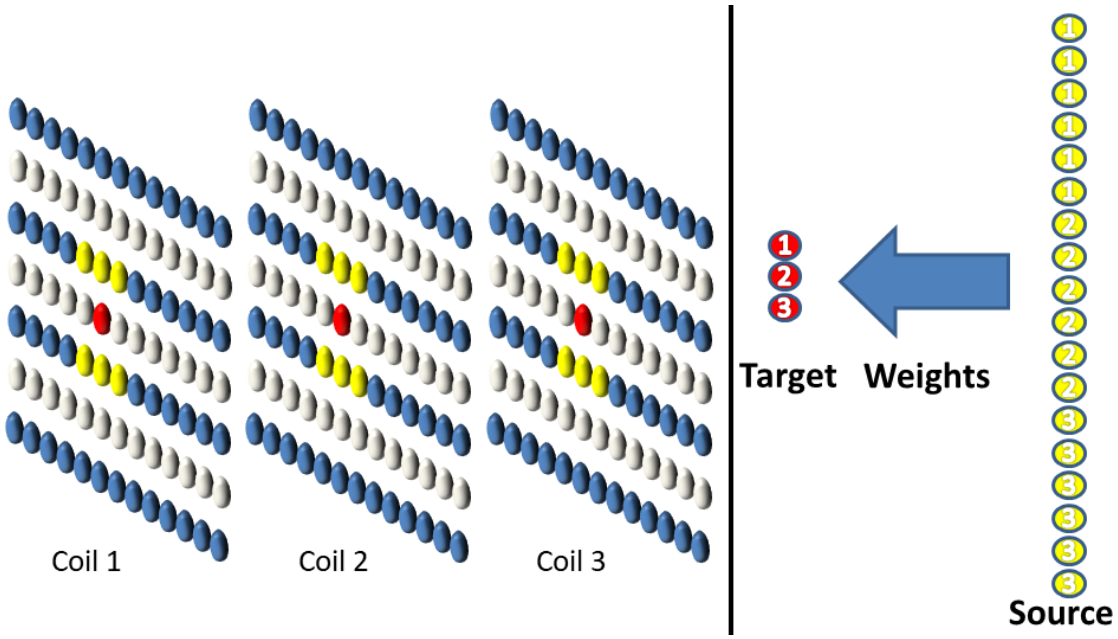

Figure 3.3: GRAPPA kernel and reconstruction arrangement. 3 coil dimensions are displayed. The same kernel is swept through the k-space (left side) and at each k-space position a source and target vector are generated (right side).

$$\mathbf{S}_{target} = \mathbf{w}\mathbf{S}_{source} \tag{3.11}$$

$$\mathbf{w} = \mathbf{S}_{target}\mathbf{S}_{source,p}^{-1} = \mathbf{S}_{target}\mathbf{S}_{source}^{\dagger}(\mathbf{S}_{source}\mathbf{S}_{source}^{\dagger})^{-1} \tag{3.12}$$

Once the missing data is synthesized for each receiver coil separately, the individual receiver channel images are acquired by a simple inverse Fourier transform

and the final image is obtained by e.g. the sum-of-square images of each receiver channels.

In clinical practice, GRAPPA has overcome its predecessor, SENSE, due to its numerous advantages. First of all, the *explicit* knowledge of sensitivity maps is not required for the reconstruction. Secondly, no further measurement protocol must be introduced apart from the conventional scan, as the nature of the ACS and the data of accelerated measurement is alike. Furthermore, the typical ACS region is the central region of k-space, which contains the largest amount of frequency information when it comes to natural images. Not only can signal maximization be achieved by the right choice of ACS, but the ACS dataset can later on be inserted into the synthesized k-space to ameliorate image quality. Depending on manufacturers and user setups, ACS dataset can be measured as a prescan, or during the accelerated measurement without skipping the central k-space region.

3.3 Noise Amplification in pMRI

As discussed in the previous sections, pMRI has numerous advantages, however acceleration cannot remain unpunished. Decreased SNR is the price to pay. The diminishing of SNR is due to two independent factors: an intrinsic lessening in SNR as a result of incomplete k-space coverage and noise amplification generated by the reconstruction.

Numerous sources of noise can occur in an MRI experiment. The most straightforward distinction between noise sources is systematic and random noise. Systematic noise commonly originates from hardware fault. Random noise can emerge from physiological processes, i.e. patient movement, breathing, swallowing, blood circulation, etc. The investigation of such effects on image quality is beyond this thesis. Nevertheless, no matter how well monitored a scan is, thermal noise will always be present. Thus, discussion introduced herein is narrowed down to thermal noise. We aspire to derive the effect of thermal noise, that is present in raw k-space signal, on the final image noise.

Let $S(k)$ denote the raw k-space signal, $\tilde{S}(k)$ the ideal, noiseless k-space signal and $\epsilon(k)$ the k-space noise.

$$S(k) = \tilde{S}(k) + \epsilon(k) \tag{3.13}$$

Regularly, the final image is the inverse Fourier transform of the signal, that is

$$I(x) = \mathcal{F}^{-1}(S(k)) = \mathcal{F}^{-1}(\tilde{S}(k)) + \mathcal{F}^{-1}(\epsilon(k)) = \tilde{I}(x) + \eta(x) \tag{3.14}$$

where the linearity of the Fourier transform is adopted [6]. $I(x), \tilde{I}(x), \eta(x)$ stand for the image, the ideal image and the image-space noise, respectively.

Thermal noise is approximately *white*, which means that the power spectral density is nearly constant throughout the frequency spectrum [7]. When limited to a finite bandwidth, thermal noise amplitude can be approximated with a Gaussian distribution [7], such as $\epsilon(k) \sim \mathcal{N}(0, \sigma_m^2)$.

Practical realization of measurement operates with discrete sampling. Δk denotes the step of discrete sampling in k-space, while Δx denotes the step of discrete sampling in image-space. The variance of the discrete-valued white noise yields

$$\left\langle \epsilon(k_p)\epsilon^*(k_q) \right\rangle = \sigma_m^2 \delta_{pq} \tag{3.15}$$

where $k_p = p\Delta k$ and $k_q = q\Delta k$. Plugging in the definition of discrete inverse Fourier transforme [10] into the definition of image-space noise, we find

$$\eta(p\Delta x) = \frac{1}{N_{acq}} \sum_{p'=0}^{N_{acq}} \epsilon(p'\Delta k) e^{i2\pi p'\Delta k p \Delta x} \tag{3.16}$$

The expectation value of Equation 3.16 yields

$$\left\langle \eta(p\Delta x) \right\rangle = \frac{1}{N_{acq}} \sum_{p'=0}^{N_{acq}} \underbrace{\left\langle \epsilon(p'\Delta k) \right\rangle}_{\text{0 for all p'}} e^{i2\pi p'\Delta k p \Delta x} = 0 \tag{3.17}$$

Equation 3.17 shows that the expectation value of the noise in image-space is zero, meaning that there is no systematic noise originated from the thermal noise. Now taking the variance of both sides of Equation 3.17, we get

$$\left\langle \eta(p'\Delta x)\eta^*(q'\Delta x) \right\rangle = \sigma_{im}^2 = \tag{3.18}$$

$$= \frac{1}{N_{acq}^2} \sum_{p'=0}^{N_{acq}} \sum_{q'=0}^{N_{acq}} \underbrace{\left\langle \epsilon(p'\Delta k)\epsilon^*(q'\Delta k) \right\rangle}_{=\sigma_m^2 \delta_{p'q'}} e^{i2\pi p \Delta x (p'\Delta k - q'\Delta k)}$$

$$= \frac{\sigma_m^2}{N_{acq}^2} \sum_{p'=0}^{N_{acq}} \sum_{q'=0}^{N_{acq}} \delta_{p'q'} e^{i2\pi p \Delta x (p'\Delta k - q'\Delta k)} = \frac{\sigma_m^2}{N_{acq}} \tag{3.19}$$

Equation 3.19 states that the variance of image-space noise σ_{im}^2 is N_{acq} times smaller than the variance of k-space noise σ_m^2, meaning that every voxel of the final image is burdened with $\sqrt{N_{acq}}$ times smaller noise than the corresponding k-space

voxel. Considering the case of an accelerated acquisition, when only N_{acq}/R part of the original k-space is acquired, we find that the reconstructed image of the accelerated measurement contains $\sqrt{R}$ times greater noise compared to a conventional scan.

$$\sigma_{im}^2 = \frac{\sigma_m^2}{N_{acq,R}} = \frac{\sigma_m^2}{N_{acq}/R} = R\frac{\sigma_m^2}{N_{acq}} \tag{3.20}$$

The voxel-wise noise level is quantified by SNR, defined as the mean values of the signal divided by the standard deviation of the noise (Equation 3.21).

$$\mathrm{SNR} = \frac{E[S]}{\sigma_{\mathrm{N}}} \tag{3.21}$$

Expressing the same result of Equation 3.20 via the SNR, we find

$$SNR_R \propto \frac{SNR_{R=1}}{\sqrt{R}} \tag{3.22}$$

Beyond the above described intrinsic phenomena, further complication arises when it comes to Parallel Imaging. Due to the overlapping sensitivity profiles and remaining aliasing, an additional reduction in SNR occurs, which is represented by the so-called *geometric factor* (g-factor), as denoted in Equation 3.23. G-factor depends on coil noise and also takes into consideration the electromagnetic coupling between coils.

$$SNR_R = \frac{SNR_{R=1}}{g\sqrt{R}} \tag{3.23}$$

The upcoming sections aspire to investigate the respective g-factor of SENSE & GRAPPA offering further insight to the specific features of both techniques.

3.3.1 SENSE g-factor

Consider the final image ($\mathbf{I}$) which is composed of the inherent, noiseless image ($\tilde{\mathbf{I}} = \mathbf{C}\boldsymbol{\rho}$), as described by Equation 3.6, and the image noise ($\boldsymbol{\eta}$).

$$\mathbf{I} = \mathbf{C}\boldsymbol{\rho} + \boldsymbol{\eta} \tag{3.24}$$

An SNR-optimal solution demands that the noise covariance between receiver channels be taken into consideration. Let us assume white noise in each receiver channel, such as thermal noise, i.e. noise represented with normal distribution ($\sim \mathcal{N}(\mu, \sigma^2)$). The noise covariance matrix can be written as

$$\boldsymbol{\Psi} = \left\langle (\boldsymbol{\eta} - \langle \boldsymbol{\eta} \rangle)(\boldsymbol{\eta} - \langle \boldsymbol{\eta} \rangle)^\dagger \right\rangle = \left\langle (\boldsymbol{\eta}\boldsymbol{\eta}^\dagger \right\rangle \tag{3.25}$$

where † denotes the Hermitian adjoint i.e. conjugate transpose.

Equation 3.26 denotes the quadratic function that needs to be minimized to achieve an SNR-optimal solution [12].

$$F = (\mathbf{I} - \mathbf{C}\boldsymbol{\rho})^{\dagger}\boldsymbol{\Psi}^{-1}(\mathbf{I} - \mathbf{C}\boldsymbol{\rho}) \tag{3.26}$$

Ideal image reconstruction algorithm (Equation 3.7) is modified when image noise is taken into account (Equation 3.27). Please be aware that Equation 3.7 is a special case of Equation 3.27, once setting $\boldsymbol{\Psi} = \mathbb{1}$, that is, accepting the hypothesis of independently identically distributed (IID) receiver channel noise.

$$\boldsymbol{\rho}_{recon} = (\mathbf{C}^{\dagger}\boldsymbol{\Psi}^{-1}\mathbf{C})^{-1}\mathbf{C}^{\dagger}\boldsymbol{\Psi}^{-1}\mathbf{I} \tag{3.27}$$

Consequently, reconstruction noise propagates the same way as the modified reconstruction.

$$\boldsymbol{\eta} = (\mathbf{C}^{\dagger}\boldsymbol{\Psi}^{-1}\mathbf{C})^{-1}\mathbf{C}^{\dagger}\boldsymbol{\Psi}^{-1}\boldsymbol{\epsilon} \tag{3.28}$$

Respecting the recent findings, let us derive the variance of image noise.

$$\begin{aligned}\sigma^2_{recon} = \left\langle \boldsymbol{\eta}\boldsymbol{\eta}^{\dagger} \right\rangle = \left\langle [(\mathbf{C}^{\dagger}\boldsymbol{\Psi}^{-1}\mathbf{C})^{-1}\mathbf{C}^{\dagger}\boldsymbol{\Psi}^{-1}\boldsymbol{\eta}][(\mathbf{C}^{\dagger}\boldsymbol{\Psi}^{-1}\mathbf{C})^{-1}\mathbf{C}^{\dagger}\boldsymbol{\Psi}^{-1}\boldsymbol{\eta}]^{\dagger} \right\rangle = \\ = (\mathbf{C}^{\dagger}\boldsymbol{\Psi}^{-1}\mathbf{C})^{-1}\mathbf{C}^{\dagger}\boldsymbol{\Psi}^{-1}\underbrace{\left\langle \boldsymbol{\eta}\boldsymbol{\eta}^{\dagger} \right\rangle}_{\boldsymbol{\Psi}}\boldsymbol{\Psi}^{-1}\mathbf{C}^{\dagger}(\mathbf{C}^{\dagger}\boldsymbol{\Psi}^{-1}\mathbf{C})^{-1} = (\mathbf{C}^{\dagger}\boldsymbol{\Psi}^{-1}\mathbf{C})^{-1}\end{aligned}$$

Adopting the result of the standard deviation of image noise into the definition of g-factor (Equation 3.23), we get

$$g_k = \frac{\sigma_{recon,R}}{\sigma_{recon,R=1}} = \frac{\sqrt{[(\mathbf{C}^{\dagger}\boldsymbol{\Psi}^{-1}\mathbf{C})^{-1}_{R}]_{k,k}}}{\sqrt{[(\mathbf{C}^{\dagger}\boldsymbol{\Psi}^{-1}\mathbf{C})^{-1}_{R=1}]_{k,k}}} \tag{3.29}$$

Reformulating Equation 3.29, we find the exact direction of g-factor computation.

$$g_k = \sqrt{[(\mathbf{C}^{\dagger}\boldsymbol{\Psi}^{-1}\mathbf{C})^{-1}_{R}]_{k,k}[(\mathbf{C}^{\dagger}\boldsymbol{\Psi}^{-1}\mathbf{C})_{R=1}]_{k,k}} \tag{3.30}$$

3.3.2 GRAPPA g-factor

A different approach is required for the derivation of GRAPPA g-factor. As g-factor describes the spatial distribution of noise amplification on the final image, the previously introduced quantities of GRAPPA reconstruction must be translated into image-space from k-space. An alternative GRAPPA reconstruction is presented while the derivation of GRAPPA g-factor is deduced. Herein lies the difficulty of

GRAPPA g-factor computation.

The schematic derivation of image-space kernel (**W**) is depicted in Figure 3.4. At a given relative position $l-n$ the kernel weights are extracted from the source dataset. The kernel is flipped in both dimension, then zero padded to reach the dimensions of the reconstructed image, finally an inverse Fourier transform is performed on it. It is noteworthy that the kernel weights keep their relative position with respect to one another throughout these transformations, which ensures that the information associated with the relative coordinate $l - n$ is still encoded in the image-space kernel.

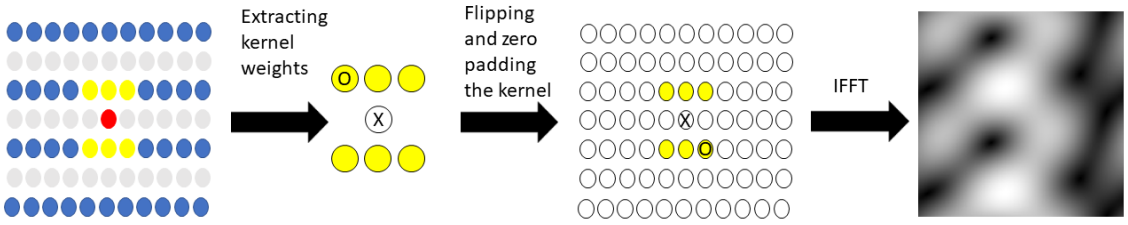

Figure 3.4: [14] Derivation of image-space GRAPPA kernel. k-space kernel (w) is flipped in both dimension, then zero padded to reach the dimensions of the reconstructed image, finally an inverse Fourier transform is performed on it. Image space kernel (W) is derived. The procedure is repeated N^2 times to compute all image-space kernels from original N^2 k-space kernels.

Using the definition of convolution, the original k-space-based GRAPPA reconstruction (Equation 3.10) can be rewritten into Equation 3.31. In image-space, Equation 3.10 can be reinterpreted as a voxel-wise multiplication in image-space of the overlapping images and the inverse Fourier transform of the adequate kernel. Image-space GRAPPA reconstruction is reformulated in Equation 3.32. The relative coordinates of k-space position $l - n$ have been omitted from Equation 3.32 as $l - n$ have been used at the derivation of image-space kernels. Please note that w and W denote kernels in k-space and image-space, respectively and the number of kernels remain N^2 independently of the chosen representation.

$$S_j = \sum_{m=1}^{N} w_{j,m} * S_m \tag{3.31}$$

$$I_j = \sum_{m}^{N} W_{j,m} \cdot I_m \tag{3.32}$$

Consider the final image of the j-th individual receiver channel (I_j) which is composed of the inherent, noiseless image ($\tilde{I}_j$) and the image noise (η_j).

$$I_j = \tilde{I}_j + \eta_j = \sum_m^N W_{j,m} \cdot (\tilde{I}_m + \eta_m) \tag{3.33}$$

Transitioning into vector and matrix formalism for all receiver channels, we find

$$\mathbf{I} = \tilde{\mathbf{I}} + \boldsymbol{\eta} = \mathbf{W}(\mathbf{I} + \boldsymbol{\eta}) \tag{3.34}$$

The variance of the image noise is computed as follows

$$\begin{aligned} \sigma^2_{recon} &= \left\langle \boldsymbol{\eta}^{recon} \boldsymbol{\eta}^{recon\dagger} \right\rangle = \left\langle (\mathbf{W}\boldsymbol{\eta})(\mathbf{W}\boldsymbol{\eta})^\dagger \right\rangle = \\ &= \mathbf{W} \left\langle \boldsymbol{\eta}\boldsymbol{\eta}^\dagger \right\rangle \mathbf{W}^\dagger = \mathbf{W}\boldsymbol{\Psi}\mathbf{W}^\dagger \end{aligned} \tag{3.35}$$

Contrary to SENSE, GRAPPA reconstruction algorithm return images separately for every receiver channel. Thus, g-factors are computed separately for every voxel of every receiver channel. According to definition, g-factor is the fraction of image noise of the accelerated and non-accelerated image. G-factor for the j-th coil yields

$$g_j = \frac{\sigma_{recon,R}}{\sigma_{recon,R=1}} = \frac{\sqrt{[(\mathbf{W}\boldsymbol{\Psi}\mathbf{W}^\dagger)_R]_{j,j}}}{\sqrt{[(\boldsymbol{\Psi})_{R=1}]_{j,j}}} \tag{3.36}$$

Individual g-factors are combined using the same combination weights as for the combination of the individual images for reconstruction.

$$I^{final} = \sum_{j=1}^N p_j I_j^{recon} = \mathbf{p}^T \mathbf{I}^{recon} \tag{3.37}$$

For a conventional sum-of-squares (SOS) combination the combination weights are defined as [18]

$$p_j = \frac{I_j^*}{I_{SOS}} \tag{3.38}$$

Applying the combination weights on the image noise ($\boldsymbol{\eta}$), the variance of the image noise yields

$$\begin{aligned} \sigma^2_{final} &= \left\langle \boldsymbol{\eta}^{final} \boldsymbol{\eta}^{final\dagger} \right\rangle = \left\langle (\mathbf{p}^T\mathbf{W}\boldsymbol{\eta})(\mathbf{p}^T\mathbf{W}\boldsymbol{\eta})^\dagger \right\rangle = \\ &= \mathbf{p}^T\mathbf{W} \left\langle \boldsymbol{\eta}\boldsymbol{\eta}^\dagger \right\rangle \mathbf{W}^\dagger\mathbf{p}^* = \mathbf{p}^T\mathbf{W}\boldsymbol{\Psi}\mathbf{W}^\dagger\mathbf{p}^* \end{aligned} \tag{3.39}$$

Inserting the results into Equation 3.36, we find

$$g_{final} = \frac{\sigma_{final,R}}{\sigma_{final,R=1}} = \frac{\sqrt{[(\mathbf{p}^T \mathbf{W} \mathbf{\Psi} \mathbf{W}^\dagger \mathbf{p}^*)_R]}}{\sqrt{[(\mathbf{p}^T \mathbf{\Psi} \mathbf{p}^*)_{R=1}]}} \tag{3.40}$$

The non-accelerated individual images from each receiver channels must be combined likewise, thus we find the denominator of Equation 3.40.

Chapter 4

Coil Compression Methods

Receiver coils with a great number of receiver channels have become available in clinical practice. Numerous advantages can be exploited by applying a great number of receiver coils, such as increased SNR or improved acceleration performance in pMRI. However, application of a large set of receiver channels generates an additional need for hardware performance and computation capacity. The more channels collect data from sample, the lengthier the reconstruction becomes.

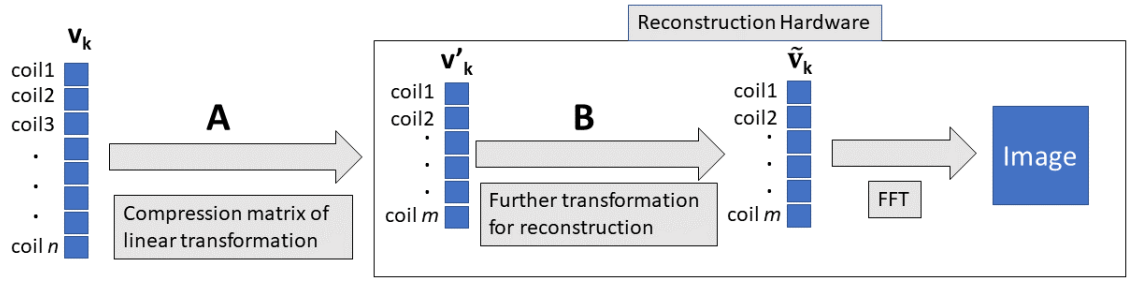

Figure 4.1: Coil Compression work-flow. CC is carried out in advance of image reconstruction. Current chapter is dedicated to the search of the linear transformation $\boldsymbol{A}$ *that executes the CC for diverse pMRI techniques.*

Coil Compression (CC) methods allow reducing computation time by transforming and combining raw k-space datasets prior to sending them to reconstruction hardware, as illustrated on Figure 4.1. The core of CC algorithms is to compress data from many physical channels into fewer virtual channels while minimizing the SNR loss. Overlapping coil sensitivities in the folded ROI do not form an orthogonal basis and often span a subspace whose dimension is considerably smaller than the number of physical coils [15][16] resulting in a huge amount of redundant and highly correlated data.

Realization of CC methods may differ from one another but the basic concept is identical. The key is that a linear transformations is applied on raw k-space datasets. New set of virtual coils are generated from the original set of physical coils by exploiting the singular value decomposition of linear algebra. A supplementary

linear transformation may be applied to ensure spatial smoothness of virtual coil sensitivities.

4.1 Coil Compression Methods

Let $\mathbf{v_k}$ denote raw k-space data from all N physical receiver coils of a given coordinate $\mathbf{k}$. CC is achieved by a linear transformation represented by matrix $\mathbf{A}$ with dimensions $m \times n$. Mathematically, CC can be formulated as follows

$$\mathbf{v'_k} = \mathbf{A}\mathbf{v_k} \tag{4.1}$$

Throughout this section, one is in search of linear transformation $\mathbf{A}$.

It has been shown in the previous chapter that the image noise in the unfolded voxel $\mathbf{k}$ after an R-times accelerated measurement, described by the g-factor of SENSE in Equation 3.30, can be expressed as follows

$$\sigma^2_{recon,R} = [(\mathbf{C}^\dagger_\mathbf{k}\mathbf{\Psi}_n^{-1}\mathbf{C_k})^{-1}_R]_{k,k} \tag{4.2}$$

where $\mathbf{C_k}$ denotes the superimposed coil sensitivities from all coil in the superimposed voxel $\mathbf{k}$, $\mathbf{\Psi}$ stands for the noise covariance of all receiver coils. One aims to minimize noise propagation enhancement magnified by CC, i.e. fulfill the criteria $\sigma^2_{recon,R} = \min$.

Let us perform the linear transformation $\mathbf{A}$ on the overlapping sensitivity matrix $\mathbf{C_k}$, which likewise affects the noise covariance matrix $\mathbf{\Psi}$.

$$\mathbf{C'_k} = \mathbf{A}\mathbf{C_k} \qquad \mathbf{\Psi}_m = \mathbf{C'_k}\mathbf{C'^\dagger_k} = \mathbf{A}\mathbf{\Psi}_n\mathbf{A}^\dagger \tag{4.3}$$

Inserting Equation 4.3 into Equation 4.2, it yields

$$\sigma^{2'}_{recon,R} = [(\mathbf{C}^\dagger_\mathbf{k}\mathbf{A}^\dagger(\mathbf{A}\mathbf{\Psi}_n\mathbf{A}^\dagger)\mathbf{A}\mathbf{C_k})^{-1}_R]_{k,k} = \min \tag{4.4}$$

Minimization of the image noise in the whole folded ROI can be carried out by the summation of minimized image noise in each voxel $\mathbf{k}$.

$$\sum_{\mathbf{k}\in ROI_{folded}} \sigma^2_{recon,R} = \sum_{\mathbf{k}\in ROI_{folded}} [(\mathbf{C}^\dagger_\mathbf{k}\mathbf{A}^\dagger(\mathbf{A}\mathbf{\Psi}_n\mathbf{A}^\dagger)\mathbf{A}\mathbf{C_k})^{-1}_R]_{k,k} \tag{4.5}$$

One demands that the newly generated m virtual coils be decorrelated, i.e. the noise covariance matrix of the m virtual coils $\mathbf{\Psi}_m$ be equal to identity $\mathbb{1}$.

$$\mathbf{\Psi}_m = \mathbf{A}\mathbf{\Psi}_n\mathbf{A}^\dagger = \mathbb{1} \tag{4.6}$$

Let us define transformation $\mathbf{T}$ which acts on the raw dataset as follows

$$\hat{\mathbf{\Psi}}_n = \mathbf{T}\mathbf{\Psi}_n\mathbf{T} = \mathbb{1} \tag{4.7}$$

Transformation $\mathbf{T}$ executes coil noise whitening, i.e. renders linearly independent the separate receiver channels.

Substituting the whitened noise covariance matrix, described by Equation 4.7, into the constraint for the newly derived m virtual coils, mathematically reformulated by Equation 4.6, one finds

$$\mathbf{\Psi}_m = \mathbb{1} = \mathbf{A}\hat{\mathbf{\Psi}}_n\mathbf{A}^\dagger = \mathbf{A}\mathbf{A}^\dagger \tag{4.8}$$

One can declare that the constraint for the m virtual coil elements to be decorrelated (Equation 4.6) translates into the constraint for $\mathbf{A}$ to be unitary (Equation 4.9) [15][16].

$$\mathbf{A}\mathbf{A}^\dagger = \mathbb{1} \tag{4.9}$$

Acknowledging the freshly derived result, one can establish requirements for Coil Compression algorithms. When applying Coil Compression, one aims to minimize image noise propagation enhancement (Equation 4.10), which is identical to maximizing the SNR in the entire ROI by maximizing the superimposed coil sensitivity in all voxels (Equation 4.11). Independently form the above-mentioned reformulation, constraint for $\mathbf{A}$ to be unitary holds. Equation 4.10 and Equation 4.11 are equal as they can be easily transformed into one another with simply taking the inverse, as denoted below. Equation 4.10 and Equation 4.11 are derived by substituting Equation 4.9 into Equation 4.5.

$$\sum_{\mathbf{k}\in ROI_{folded}} \sigma^2_{recon,R} = \sum_{\mathbf{k}\in ROI_{folded}} [(\mathbf{C}^\dagger_{\mathbf{k}}\mathbf{A}^\dagger\mathbf{A}\mathbf{C}_{\mathbf{k}})^{-1}_R]_{k,k} = \min \tag{4.10}$$

$$\sum_{\mathbf{k}\in ROI_{folded}} \frac{1}{\sigma^2_{recon,R}} = \sum_{\mathbf{k}\in ROI_{folded}} [(\mathbf{C}^\dagger_{\mathbf{k}}\mathbf{A}^\dagger\mathbf{A}\mathbf{C}_{\mathbf{k}})_R]_{k,k} = \max \tag{4.11}$$

$$\text{subject to } \mathbf{A}^\dagger\mathbf{A} = \mathbb{1}$$

Computation of the aforementioned equations is demanding as desired linear transformation $\mathbf{A}$ is situated in the core of the equations and computational numerical iterative methods should be applied to find the extreme. Instead, an appropriate approximation of $\mathbf{A}$ can drastically simplify the problem.

Effectiveness and applicability of CC seriously relies on the approximation of $\mathbf{A}$. In the following sections, several approximative methods for SENSE & GRAPPA

are derived and compared.

4.2 CC SENSE: Principle Component Analysis & Optimized Transformation

Principle Component Analysis (PCA) is an effective method to reduce the dimensionality of a problem [20]. PCA uses a linear transformation to alter an initial dataset of possibly correlated variables into a linearly uncorrelated set of variables called principal components. Linear transformation is defined in such a way that the first principal component has the largest possible variance and each succeeding component has the highest variance possible under the constraint that it is orthogonal to the preceding components [20]. Thus, the set of principle components form an orthogonal basis.

Intuitively, PCA can be thought of as revealing the internal structure of the data in a way that best explains the variance in the data. If a multivariate dataset in a high dimensional space is analyzed, PCA can supply a lower-dimensional representation, i.e. a projection from a higher dimension into a lower dimension subspace. Impulsively, the projection enables the dataset to be inspected from its most informative viewpoint [20], which is, mathematically speaking, done by selecting only the first few principal components. By omitting principle components of minor contribution to the representation, only a commensurately small amount of information is lost. This explains how the dimensionality of the transformed data is reduced.

Let us define matrix $\mathbf{Q}$.

$$\mathbf{Q} = \sum_{\mathbf{k} \in ROI_{folded}} \mathbf{C_k} \mathbf{C_k^\dagger} \tag{4.12}$$

PCA performs a singular value decomposition (SVD) [21] on matrix $\mathbf{Q}$ such that

$$\mathbf{Q} = \mathbf{V}\mathbf{F}\mathbf{V}^\dagger \tag{4.13}$$

where $\mathbf{V}$ is a unitary matrix, while $\mathbf{F}$ is a diagonal positive semi-definite matrix. As $\mathbf{Q}$ is symmetric, SVD returns a lower and upper triangular matrix that can be transformed into one another by a simple Hermitian adjoint. Since $\mathbf{V}$ is unitary, its columns form a set of orthonormal vectors, which can be regarded as orthogonal basis vectors.

SVD is a generalization of the eigenvalue decomposition of pure stretches in orthogonal directions [21]. Scaling factors of stretches of eigenvalue decomposition translates in SVD under the form of matrix $\mathbf{F}$. SVD can be composed of three successive geometrical transformation: rotation ($\mathbf{V}$), scaling ($\mathbf{F}$) and another rotation

($\mathbf{V}^\dagger$).

Approximation of matrix $\mathbf{A}$ can be effectuated if the first m rows of the unitary matrix $\mathbf{V}^\dagger$ is selected, that is, the first m rows belonging to the m largest singular values, regrouped in diagonal matrix $\mathbf{F}$, is selected. Selection is carried out by $\mathbf{D} = (id|0)$ with dimensions $m \times n$. Noise whitening matrix $\mathbf{T}$ is also incorporated into the definition of the approximation of compression transformation $\mathbf{A}_{PCA}$.

$$\mathbf{A}_{PCA} = \mathbf{D}\mathbf{V}^\dagger\mathbf{T} \tag{4.14}$$

It can be shown that $\mathbf{A}_{PCA}$ maximizes the sum defined by Equation 4.11 [15], that is PCA maximizes the total amount of sensitivity in generated set of virtual coils.

The herein derived $\mathbf{A}_{PCA}$ has one major fault: not only does it include weighting according to the phase, but also according to the length of the sensitivity matrices in a voxel [15]. Accordingly, PCA prefers voxels with high sensitivity over voxels with low sensitivity, and therefore results in inhomogeneous virtual sensitivity maps. To provide a clearer point on this major drawback, let us consider the following example. Let $\mathbf{A}_{PCA}$ be such that a single voxel in the combined virtual sensitivity map receives zero sensitivity. Due to the inversion in the images noise formula (SENSE g-factor formula described by Equation 3.30), this very voxel becomes a singularity and contributes an infinite noise amplification term to image noise, which is utmost undesirable.

A solution to the problem can be achieved by redefining Equation 4.12 with minding the orthonormalization of the superimposed sensitivity maps, as shown in Equation 4.15. Orthonormalization is the key difference between PCA and the optimized transformation (OPT). Consequently, angular differences of the superimposed sensitivity matrices are taken into account, whereas the lengths are not. As a result, a more homogeneous virtual sensitivity map can be achieved as all voxels are treated identically.

By definition, applying the Moore-Penrose pseudoinverse instead of the simple Hermitian adjoint in Equation 4.12, the vector lengths are omitted from consideration as can be seen in Equation 4.15. $\mathbf{P}$ carries all desired features of $\mathbf{Q}$ without taking into account the squared length of the overlapping sensitivity maps. Only the relative phase is considered, which ensures a more homogeneous virtual sensitivity map.

$$\mathbf{P} = \sum_{\mathbf{k}\in ROI_{folded}} \mathbf{C}_\mathbf{k}\mathbf{C}_{\mathbf{k},p}^{-1} = \sum_{\mathbf{k}\in ROI_{folded}} \mathbf{C}_\mathbf{k}\mathbf{C}_\mathbf{k}^\dagger(\mathbf{C}_\mathbf{k}\mathbf{C}_\mathbf{k}^\dagger)^{-1} \tag{4.15}$$

Afterwards, SVD and the definition of the optimized coil compression matrix

goes likewise as described above.

$$\mathbf{P} = \mathbf{U}\mathbf{G}\mathbf{U}^{\dagger} \tag{4.16}$$

$$\mathbf{A}_{OPT} = \mathbf{D}\mathbf{U}^{\dagger}\mathbf{T} \tag{4.17}$$

4.3 CC GRAPPA: Geometric-decomposition Coil Compression

So far coil compression based on SNR maximization has been considered. The *explicit* knowledge of coil sensitivities to maximize SNR in the folded ROI have been exploited. This type of coil compression is suitable for sensitivity-based PI reconstructions like SENSE. On the other hand, data-based PI techniques, such as GRAPPA, do not require the *explicit* knowledge of sensitivity maps, thus require a slightly different approach for CC derivation. It is noteworthy that the presence of spatially varying sensitivity maps is crucial for data-based PI, thus *implicit* knowledge of sensitivity maps is still required.

Noise covariance of different receiver channels is taken into consideration. Noise whitening is performed on raw k-space data, thus the noise becomes independently identically distributed (IID) prior to any other transformation.

Since the readout direction is fully sampled in most in-plane PI techniques [12], the spatial variation of sensitivity maps along this direction is not utilized for the acceleration. Thus, at every location x, a two dimensional subspace $\mathbf{v_x}(\mathbf{k_y}, \mathbf{k_z})$ of $(\mathbf{k_y}, \mathbf{k_z})$ data can be created [16]. Coil Compression is performed in the $(\mathbf{k_y}, \mathbf{k_z})$ all along the x-axis.

Geometric-decomposition Coil Compression (GCC) algorithm can be formulated as a minimization problem of Equation 4.18. One demands that $\mathbf{A_x}$ be unitary at every location x, which serves as constraint.

$$\begin{aligned} &min \sum_{x,k_y,k_z} ||(\mathbf{A_x}^{\dagger}\mathbf{A_x} - \mathbb{1})\mathbf{v_x}(\mathbf{k_y}, \mathbf{k_z}||^2 \\ &\text{subject to } \mathbf{A_x}^{\dagger}\mathbf{A_x} = \mathbf{I} \end{aligned} \tag{4.18}$$

Pseudocode of GCC is denoted below:

1. Inverse Fast Fourier Transform (IFFT) of k-space multicoil data along the readout direction into $[x, k_y, k_z]$ coordinates.

2. At each location x, construct a data matrix X_x in which each row consists of all the $\mathbf{v_x}(\mathbf{k_y}, \mathbf{k_z})$ data from all individual original coils.

3. Perform SVD of $\mathbf{X_x} = \mathbf{U_x}\mathbf{\Sigma_x}\mathbf{V_x^\dagger}$ then take the first m rows of $\mathbf{U_x}^\dagger$ to form an initial compression matrix $\mathbf{A_x}^0$

4. Repeat step 2 and 3 for all position x.

However, virtual coil sensitivity smoothness is not assured in this step. Virtual Coil Alignment is performed separately with an extra projection of the initial compression matrix $\mathbf{A_x}^0$ that have been derived for each location x.

4.3.1 Virtual Coil Alignment

Coil sensitivity smoothness is ensured in this step. The idea behind the alignment is that coil sensitivity smoothness along the RO directions is crucial as unacquired data are synthesized from data along this direction. It has been shown in previous chapters that for accurate GRAPPA weights the phase of GRAPPA ACS must not differ considerably from the phase of the actual acquisition.

New compression matrices along the RO direction ($\mathbf{A_x}$) are defined as a projection of the initial compression matrices ($\mathbf{A_x}^0$).

$$\mathbf{A_x} = \mathbf{P_x}\mathbf{A_x}^0 \tag{4.19}$$

Alignment can be achieved by the following iterative optimization.

$$\begin{aligned} &min \sum_x ||\mathbf{A_x} - \mathbf{A_{x-1}}||_F^2 \\ &\text{subject to } \mathbf{A_x} = \mathbf{P_x}\mathbf{A_x}^0 \\ &\text{where } \mathbf{P_x}\mathbf{P_x}^\dagger = \mathbf{P_x}^\dagger\mathbf{P_x} = \mathbf{I} \end{aligned} \tag{4.20}$$

where the norm $||\cdot||_F^2$ stands for the Frobenius norm [11].

Equation 4.20 does not have a unique solution [16]. $\mathbf{P_x} = \mathbf{I}$ is defined at a specific slice x for all the other slices. Assuming $\mathbf{P_1} = \mathbf{I}$, orthogonal alignment matrices $\mathbf{P_x}$ for all slices can be found sequentially.

1. Given $\mathbf{A_{x-1}}$, define $\mathbf{C_x} := \mathbf{A_x}^0\mathbf{A_{x-1}}^\dagger$

2. Perform an SVD on $\mathbf{C_x}$ such that $\mathbf{C_x} = \mathbf{U_x^C}\mathbf{\Sigma_x^C}\mathbf{V_x^{C\dagger}}$

3. Set $\mathbf{P_x} = \mathbf{V_x^C}\mathbf{U_x^{C\dagger}}$ and $\mathbf{A_x} = \mathbf{P_x}\mathbf{A_x^0}$. This $\mathbf{A_x}$ minimizes the image noise defined in Equation 3.30.

4. Repeat step 1-3 for all coordinates x for all slices.

Iterative definition of the projection, using compression matrices both at locations x and $x-1$, guarantees that the successive x locations are compressed similarly, preventing any harsh jump or distortion.

After alignment, Coil Compression can be executed. Please bear in mind that a one dimensional Fourier transform of the virtual dataset along x-axis must be performed so that the original data structure is reset.

Chapter 5

Implementation and Simulations

All of the aforementioned methods (SENSE, GRAPPA, CC SENSE & CC GRAPPA) have been implemented in MATLAB R2015a (The MathWorks Inc., Natick, MA,USA). Simulations were all performed on the 2D Shepp-Logan phantom representing a single slice of a conventional 2D scan.

Similar concept has been applied for the discussion both on SENSE and GRAPPA. Every simulation has been run with parameters denoted in Table 5.1. Please note that in-plane PI techniques demand that the number of coils be greater than or even to the acceleration factor, which has been respected throughout the simulations.[1]

Acceleration factor	Number of physical coils
2	2,4,8,12,16,20,24,32,48,64
3	4,8,12,16,20,24,32,48,64
4	4,8,12,16,20,24,32,48,64
6	8,12,16,20,24,32,48,64
8	8,12,16,20,24,32,48,64

Table 5.1: Possible simulation parameter pairs for given acceleration factors and number of physical coils.

Please note that, given the number of parameter pairs, only a few examples have been outlined and shown in this thesis. Clinically relevant parameter pairs are also more likely to be depicted in this work.

Validation of CC methods is a multistep procedure. Justification of applicability consist of the following stages: image quality observation, g-factor and noise amplification evaluation and verdict on time gain. This thesis goes through these aspects highlighting the key features to reach at a verdict on the possible applicability of CC methods.

True benefits of Coil Compression can be considered if the slice dimension is not omitted either. A conventional anatomical scan in clinical practice is composed of

[1]All of these simulations would fail at one point or another if the condition for overdetermined equations did not hold.

150-192 slices, whereas all simulations herein presented are performed on a single slice. Thus, time gain should bear an even greater impact in real life applications, as single-slice time gain results are to be multiplied by 150-192 for a more realistic picture on time gain.

5.1 Coil Compression for SENSE

A coil compression criteria was unanimously established for all CC SENSE simulations as follows. Singular values of matrices $\mathbf{Q}$ (belonging to PCA) and $\mathbf{P}$ (belonging to OPT), described by Equation 4.12 and Equation 4.15 respectively, that are lower than the 10 % of the maximal singular value of the given SVD are not taken into consideration. Thus a non-hard-coded constraint is applied as compression standard for all CC SENSE simulations.

Figure 5.1 depicts the singular values of matrices $\mathbf{Q}$ (belonging to PCA) and $\mathbf{P}$ (belonging to OPT). It is clear that the singular values of $\mathbf{P}$ decline in a faster rate than those of $\mathbf{Q}$. This difference in the decline rate is due to the dissimilar summation of sensitivities belonging to overlapping voxels. The definition of $\mathbf{P}$ utilizes the pseudoinverse for the summation (Equation 4.15), while $\mathbf{Q}$ operates only with the Hermitian adjoint of the overlapping sensitivity matrices (Equation 4.12). The latter definition results in unnormalized overlapping sensitivity maps as both the length and the phase of the complex sensitivities are taken into account in the definition of $\mathbf{Q}$ [16]. Unnormalized compression matrix $\mathbf{Q}$ brings about a smaller possible compression rate and unsmoothness in the spatial distribution of the virtual coil sensitivities. The former feature can be spotted on the gentler decline rate of singular values of $\mathbf{Q}$ compared to those of $\mathbf{P}$, while the latter feature can be detected on the apparent break of listed singular values on Figure 5.1. The aforementioned beneficial attributes of $\mathbf{P}$ over $\mathbf{Q}$ make it more suitable for coil compression.

The applicability of CC methods is largely dependent on the time gain that can be obtained. Figure 5.2 represents the change in the number of virtual coils sent to reconstruction hardware (upper row) and the time gain (lower row) with respect to the number of physical coils. Time gain is remarkable when a large set of physical coils is applied. The reconstruction time depends on the square of the coils, while the acceleration factor modifies the coefficients of the second degree polynomial. This tendency is the outcome of the 3 nested loops that happen to be the core of the reconstruction algorithm. Figure 5.3 depicts the relative time gain of CC SENSE compared to conventional SENSE for better visibility and comparability.

It is crucial to highlight that above a certain number of physical coils (N) at a given acceleration factor (R) the extent of compression saturates, i.e. the number of virtual coils becomes constant (upper row of Figure 5.2). It would be a fair statement

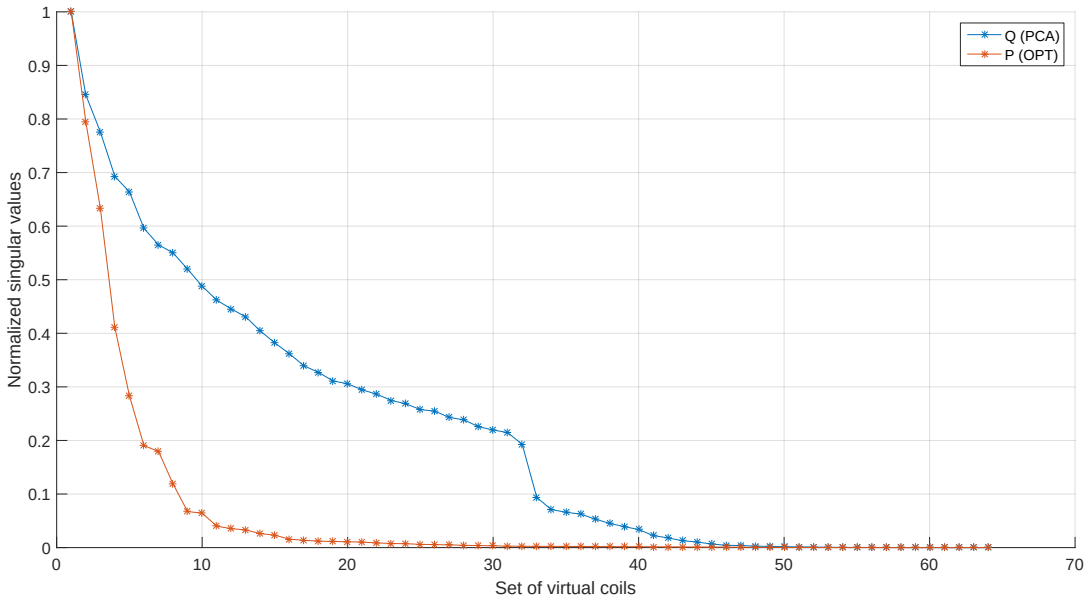

Figure 5.1: Visualization of normalized singular values of matrices $\mathbf{Q}$ *(belonging to PCA) and* $\mathbf{P}$ *(belonging to OPT). Normalization was performed so that the trends of both singular value arrays could be compared on a single plot. Simulations were performed with parameters* $R = 2$ *and* $N = 64$*. It is distinguishable that the singular values of* $\mathbf{P}$ *decline in a faster rate than those of* $\mathbf{Q}$*, which provides a better compression. Moreover, there is an unmistakable break in the continuously decreasing singular values of* $\mathbf{Q}$ *due to the unnormalized overlapping sensitivity maps.*

that, if the g-factor does not increase either once the compression has saturated, the compression algorithm has found the desired subspace spanned by the physical coils [16], i.e. the compression has reached its reasonable limit. By comparing the lower rows of Figure 5.2 and Figure 5.4, it is obvious that the trend in the g-factor change and the number of virtual coils correlates. As the number of virtual coils saturates so does the average g-factor. It is noteworthy that, while the saturation of OPT is uninterrupted, the saturation of PCA is more chaotic. The fluctuations of the latter can be justified by the same argumentation that has been previously discussed; unsmooth virtual coil sensitivities are created by the compression matrix $\mathbf{A}_{PCA}$, as it is originated from $\mathbf{Q}$ (Equation 4.14), and thus leads to diverse spatial noise amplification.

Figure 5.5 shows the geometric distributions of noise amplification for SENSE, PCA SENSE and OPT SENSE. Illustrated g-factor maps were chosen to reflect clinical applicability, as higher acceleration factors tend to result in low SNR and aliasing artifacts. It is easy to perceive that the OPT SENSE results in the highest g-factor, which may suggest high noise amplification originated from OPT compression algorithm. Nevertheless, taking into account the number of virtual coils used for the reconstruction of PCA and OPT (Figure 5.2), OPT has a considerably smaller

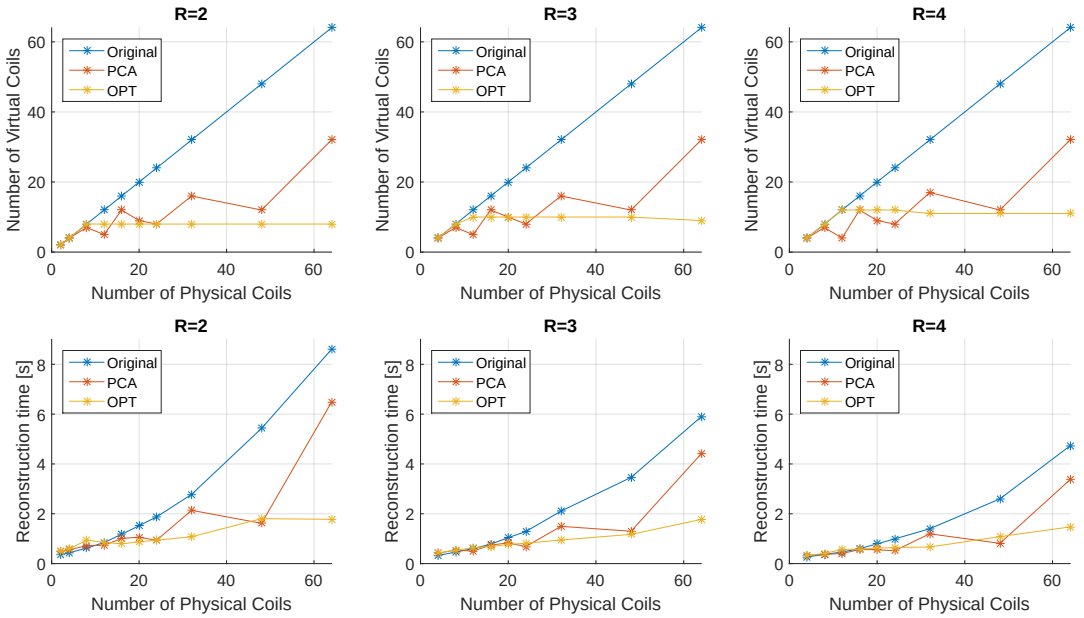

Figure 5.2: Compression factor (upper row) and reconstruction time (lower row) for CC SENSE. Upper row: the number of virtual coils generated by compression matrices $\mathbf{A}_{PCA}$ and $\mathbf{A}_{OPT}$ is shown with respect to the number of physical coils for acceleration factor $R = 2, 3, 4$. Lower row: the total reconstruction time is represented with respect to the number of physical coils. Total reconstruction time belonging to PCA and OPT were measured after CC, that is, the horizontal axis represents the original number of physical coils and not the number of virtual coils whose data was sent to reconstruction hardware.

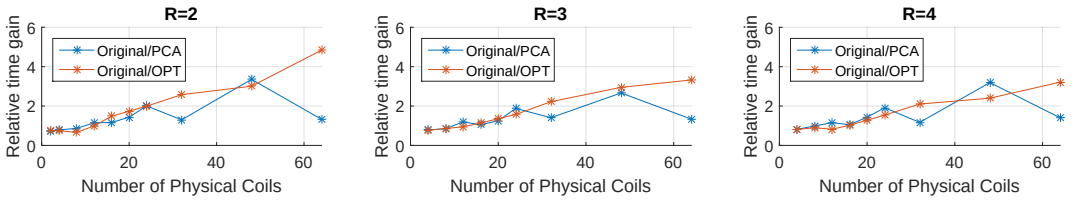

Figure 5.3: Relative time gain of CC SENSE. This figure represents the fraction of Original/PCA and Original/OPT reconstruction times that has previously been depicted on the lower row of Figure 5.2. For large sets of physical coils and low acceleration factors, which are clinically relevant cases, the relative time gain is considerable; only 1/5 (R=2) or 1/4 (R=3,4) of the original time is needed for the reconstruction.

number of virtual coils for a given acceleration factor compared to PCA. In addition, smooth virtual coil sensitivities are guaranteed for OPT SENSE, which is hardly the case for PCA SENSE. The generated virtual datasets, thus the runtime, are substantially smaller for OPT SENSE compared to PCA SENSE. As a result, a small deviation in g-factors distribution and amplitude is understandable and justified.

Figure 5.6 is achieved by the voxel-wise division of pseudo multiple replica images

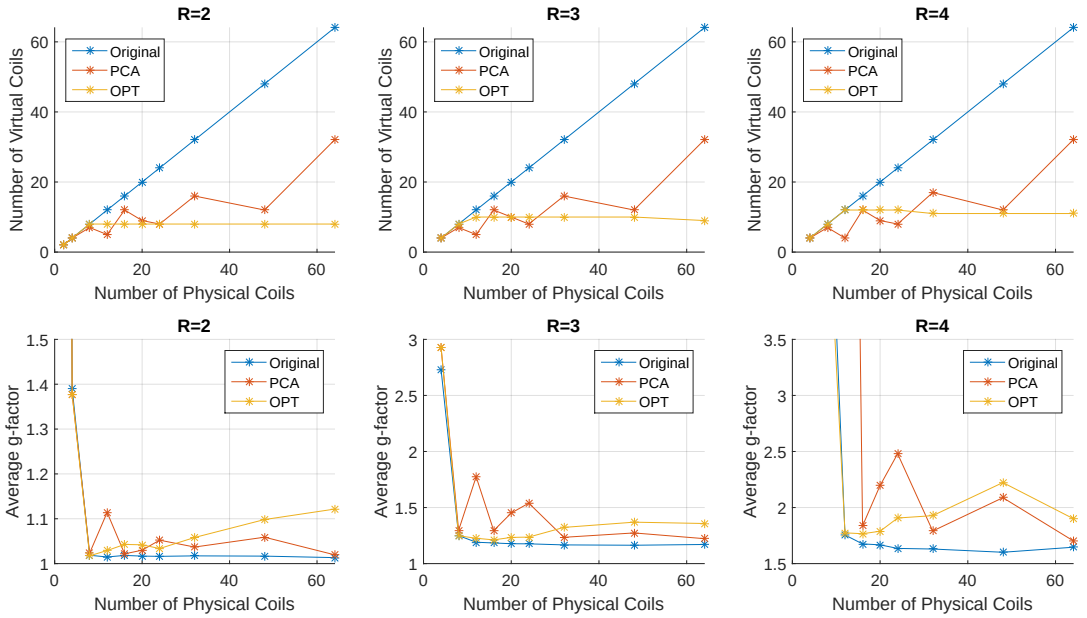

Figure 5.4: Compression factor (upper row) and average g-factor (lower row) for CC SENSE. Upper row: the number of virtual coils generated by the compression algorithm with respect to the number of physical coils. Lower row: change of the average g-factor with respect to the original number of coils. Correlation between the average g-factor and the number of virtual coils is recognizable, which serves as a justification that the compression algorithm has found the desired subspace spanned by the physical coils.

and the respective g-factors. Pseudo multiple replica images are acquired by running the same reconstruction algorithm numerous times on the same pure dataset and taking the standard deviation of all reconstructed images. Although, the dataset must be the same, a randomized Gaussian noise is added to the dataset at each loop to slightly vary initial conditions. Consequently, spatial distribution of noise amplification can be spotted. It is a simple, robust and accurate method for the quantification of SNR, but very much time-consuming [17]. Repetitions are generally set to a 100 or more. To save time and resources, g-factor, as an analytically derived method, is usually considered for SNR quantification. On the other hand, as both methods quantify the noise amplification, they can be applied to check one another. The two quantities are proportional, thus expected to return a constant spatial distribution. However, this is not the case. A spatially varying distribution attributed to the given set is returned, namely the sensitivity profile of the physical/virtual coils. It is evident that for a low compression rate the sensitivity maps are unanimous, as no considerable compression has been performed. Whereas higher compression rates result in irregular sensitivity profiles, since virtual coil sensitivities can differ considerably from the physical ones (Figure 5.6).

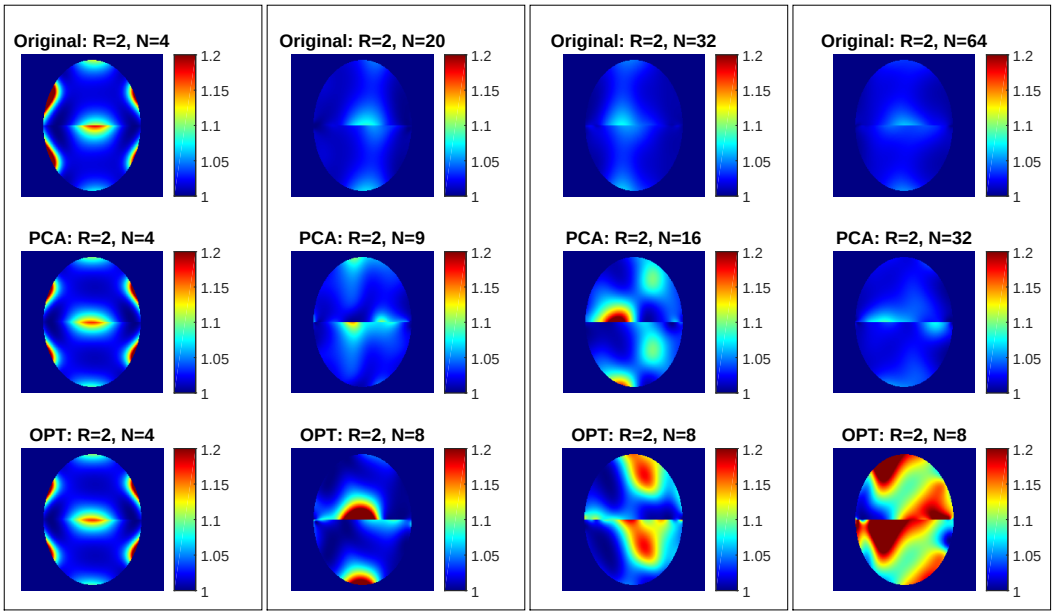

Figure 5.5: SENSE g-factor maps with and without CC. Conventional SENSE, PCA SENSE and OPT SENSE are regrouped vertically for different acceleration factors. Acceleration factor is kept constant vertically, while coil number N changes vertically due to coil compression to observe its effect on noise amplification. N indicates the number of coils whose data was sent to reconstruction hardware, i.e. for PCA SENSE and OPT SENSE N denotes the number of virtual coils.

5.2 Coil Compression for GRAPPA

Evaluation steps, introduced for CC SENSE, go likewise for CC GRAPPA. On the other hand, the unanimous coil compression criteria was modified to adapt to GCC GRAPPA structure. Singular values of matrices $\mathbf{X_x}$, described by Equation 4.18, that are lower than the 40 % of the maximal singular value of the given SVD are not taken into consideration.

Figure 5.7 shows the change in the number of virtual coils sent to reconstruction hardware (upper row) and the time gain (lower row) with respect to the number of physical coils. Not only is time gain of CC GRAPPA remarkable over conventional GRAPPA, but comparing the relative time gain of CC GRAPPA to CC SENSE (Figure 5.8 and Figure 5.3 respectively), it is even more obtrusive. The reconstruction time depends on the fourth power of the coils. This tendency is the outcome of 4 nested loops that happen to be the core of the reconstruction algorithm.

Above a certain number of physical coils (N) at a given acceleration factor (R) the extent of compression saturates, i.e. the number of virtual coils becomes constant (upper row of Figure 5.7). G-factor saturation is also experienced (Figure 5.9), henceforth, the compression has reached its reasonable limit. By comparing the lower rows of Figure 5.7 and Figure 5.9, it is obvious that the trend in the g-factor

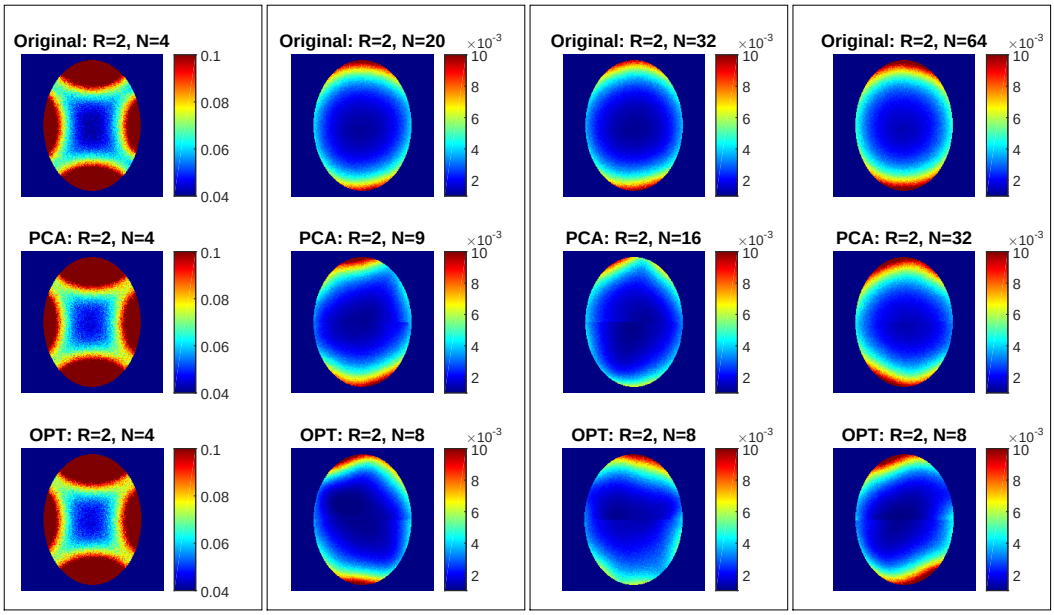

Figure 5.6: Sensitivity profiles acquired by the voxel-wise division of pseudo multiple replica images and the respective g-factors. Different cases for original SENSE, PCA SENSE and OPT SENSE are regrouped vertically. Acceleration factor is kept constant vertically, while coil number N changes vertically due to coil compression to observe its effect on sensitivity maps. N indicates the number of coils whose data was sent to reconstruction hardware, i.e. for PCA SENSE and OPT SENSE N denotes the number of virtual coils. Pseudo multiple replica images were acquired after a 100 repetitions. It is clear that the sensitivity reaches its minimum in the center region which situates the farthest from any receiver coil. The more coil is applied, the smoother the sensitivity profile is.

change and the number of virtual coils correlates. As the number of virtual coils saturates so does the average g-factor.

Figure 5.10 shows the geometric distribution of g-factors for clinically relevant acceleration factors. Undoubtedly, Coil Compression provoke noise amplification, as the spatial distribution of g-factors demonstrates. However, considering the time gain due to GCC GRAPPA, noise magnifications may be acceptable. Pseudo multiple repcila images have also been derived for GCC GRAPPA. Voxel-wise division of pseudo multiple replica images and the respective g-factors point out the underlying sensitivity maps. Figure 5.11 also demonstrates the possibly appearing artifacts, as middle regions suffer from remaining aliasing due to imperfect reconstruction.

5.3 Artifacts owing to Coil Compression

It is noteworthy that, by virtue of CC, artifacts are more likely to occur. Figure 5.12 demonstrates a few examples for conventional GRAPPA, CC GRAPPA and

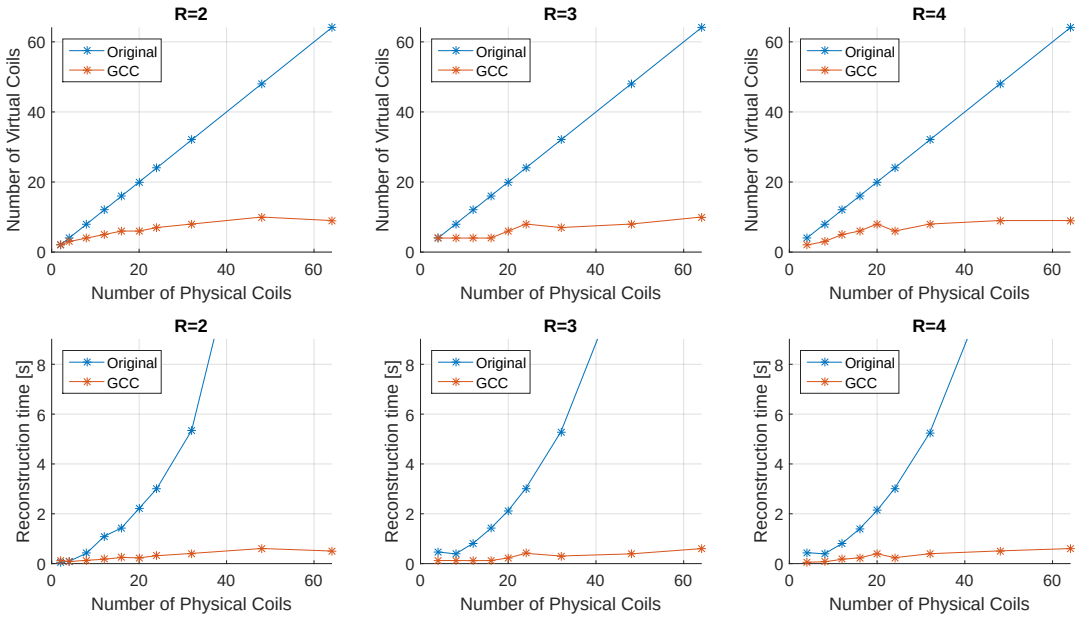

Figure 5.7: Coil compression factor (upper row) and reconstruction time (lower row) for conventional GRAPPA and GCC GRAPPA. Upper row: the number of virtual coils generated by compression matrices $\mathbf{A}_x$ is shown with respect to the number of physical coils for acceleration factor $R = 2, 3, 4$. Lower row: the total reconstruction time is represented with respect to the number of physical coils. Total reconstruction time belonging to GCC were measured after CC, that is, the horizontal axis represents the original number of physical coils and not the number of virtual coils whose data was sent to be reconstruction hardware.

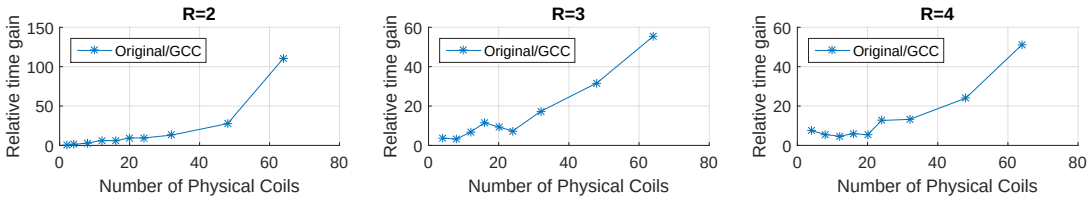

Figure 5.8: Relative time gain of GCC. This figure represents the fraction of Original/GCC reconstruction times that has previously been depicted on the lower row of Figure 5.7. For large set of physical coils and lower acceleration factors, which are clinically relevant cases, the relative time gain is considerable; only a portion of the original time is needed after CC.

difference images. Be that as it may, artifacts are not specific to CC, but rather particular GRAPPA/SENSE related artifacts are magnified as a result of CC. The effect of reduced FOV in PE direction is supposed to be eliminated by GRAPPA reconstruction, while FOV in RO direction is large enough. Henceforth, all artifacts occur in PE direction, as remaining overlapping is a considerable artifact of an imperfect reconstruction. General SNR loss is also a common side effect of CC.

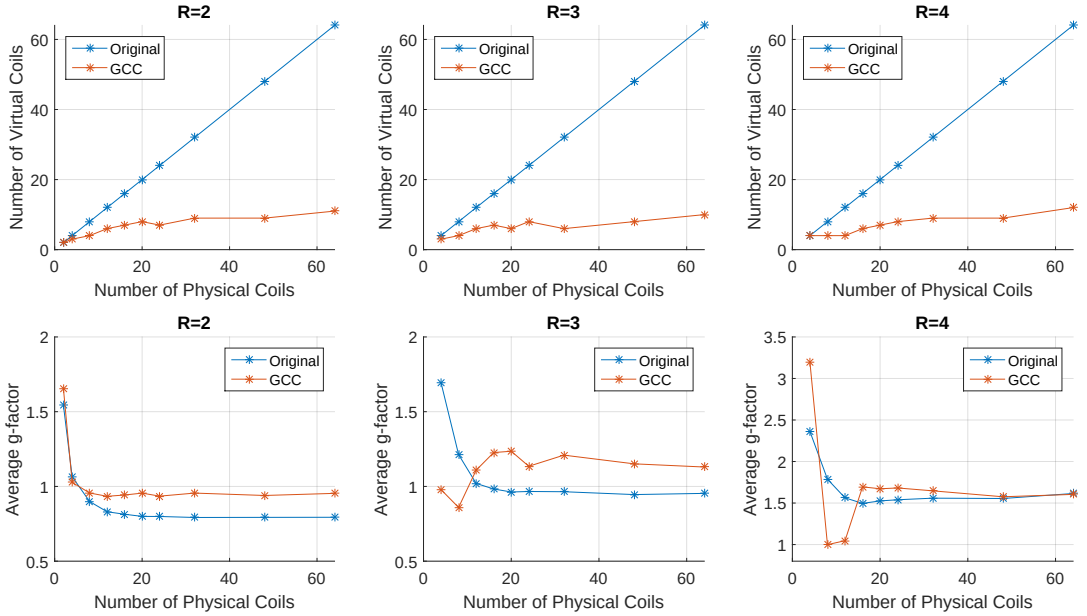

Figure 5.9: Compression factor (upper row) and average g-factor (lower row) for conventional GRAPPA and GCC GRAPPA. Upper row: the number of virtual coils generated by the compression algorithm with respect to the number of physical coils. Lower row: change of the average g-factor with respect to the original number of coils. The correlation between the two quantities is recognizable. As the number of virtual coils saturates so does the average g-factor, which means that the compression algorithm has found the desired subspace and reached its reasonable limits. The average g-factor decreases under 1, which is due to the unrealistic features of the Shepp-Logan phantom. Values of the darkest central regions, representing the cerebral aquaducts, are exactly set to zero in the analytic model, which under-represents the noise amplification in the given regions, as describes GRAPPA g-factor in Equation 3.40.

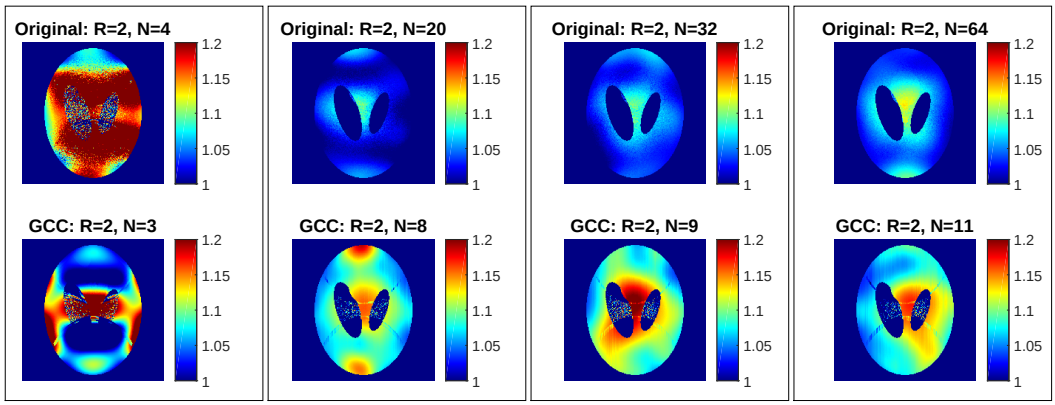

Figure 5.10: G-factor maps for conventional GRAPPA and GCC GRAPPA. G-factors are regrouped vertically for different acceleration factors. Acceleration factor is kept constant vertically, while coil number N changes vertically due to coil compression to observe its effect on noise amplification. N indicates the number of coils whose data was sent to reconstruction hardware.

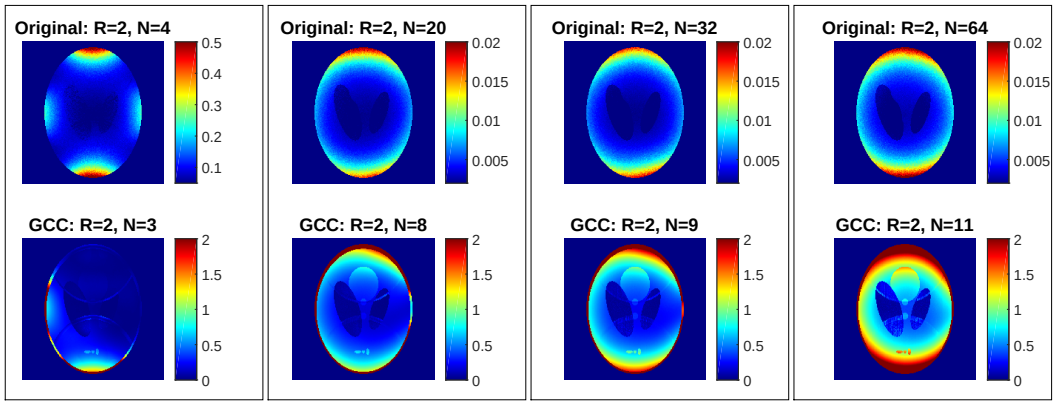

Figure 5.11: Sensitivity profiles acquired by the voxel-wise division of pseudo multiple replica images and the respective g-factors. Acceleration factor is kept constant vertically, while coil number N changes vertically due to coil compression to observe its effect on sensitivity maps. N indicates the number of coils whose data was sent to reconstruction hardware. Pseudo multiple replica images were acquired after a 100 repetitions. It is clear that the sensitivity reaches its minimum in the center region which situates the farthest from any receiver coil. Also, sensitivity maps for GCC GRAPPA indicate the presence of remaining aliasing, which is by virtue of Coil Compression.

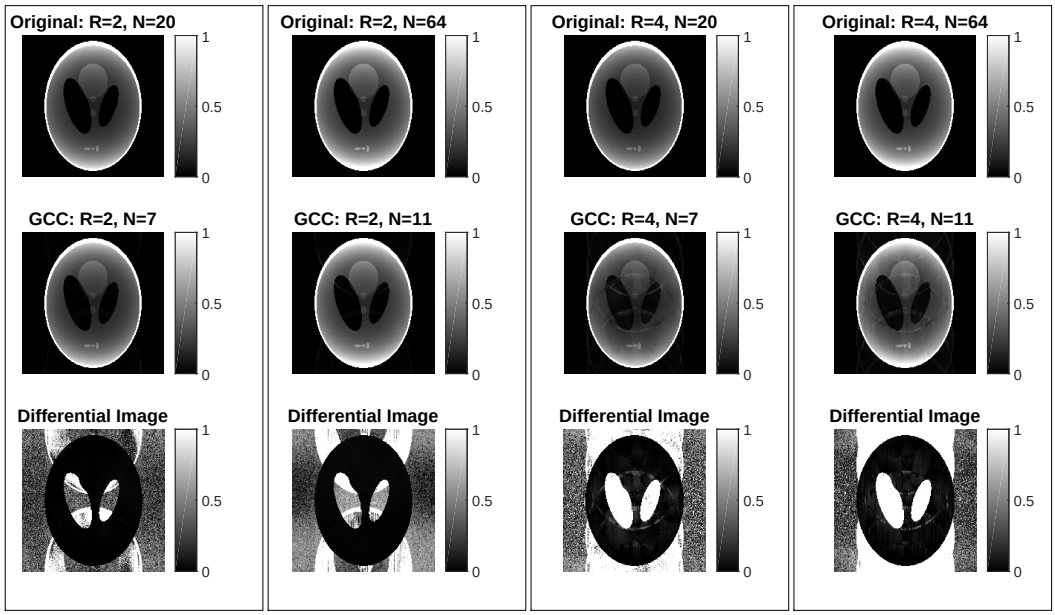

Figure 5.12: Differential images of conventional GRAPPA and GCC GRAPPA images. Acceleration factor is kept constant vertically, while coil number N changes vertically due to coil compression to observe its effect on image quality. N indicates the number of coils whose data was sent to reconstruction hardware. Normalized difference images of GCC GRAPPA and conventional GRAPPA are also displayed. It is clear that the greater the compression factor is, the more likely that artifacts occur. All artifacts emerge in the PE direction (vertical dimension) as expected.

Chapter 6

In-vivo Measurements

The very same reconstruction algorithms, whose performance has been evaluated during simulation, have been tested on real data.
All experiments were performed on a 3T clinical scanner (MAGNETOM Prisma, Siemens Healthcare, Erlangen, Germany) equipped with 20-channel head-neck receiver coils. In accordance with institutional regulations, the involved volunteer gave written informed consent before the study. All measurements were performed using built-in manufacturer sequences with a GRAPPA 2 acceleration and 16 head receiver channel on[1]. All experiments were performed at Brain Imaging Center, Research Center for Natural Sciences, Hungarian Academy of Sciences.

The following nomenclature have been introduced to apply shorter notation on displayed figures; low, optimal and moderate compression designate that 90%, 70% and 50% of the highest ranking singular values were kept for later use at the reconstruction, respectively.

The order of evaluation follows the same concept that has been presented in the previous chapter. No previously unknown quantity or method have been inaugurated in this chapter. Detailed information on the figures can be exerted from figure captions.

Figures are regrouped into two according to anatomical planes. Figure 6.1 shows a T1-weighted anatomical brain images on the transverse plane, whereas Figure 6.4 displays the coronal plane of the same volunteer. All offline reconstructed images with and without CC and all figures herein displayed have been reconstructed and generated by my own algorithms, except for reference images. Reference images reconstructed by vendor's image reconstruction software have been imported from DICOM format and read in by MATLAB.

[1] 4 receiver channels situated in the neck region were disabled, as their signal due to their spacial location does not contribute considerably to the chosen ROI.

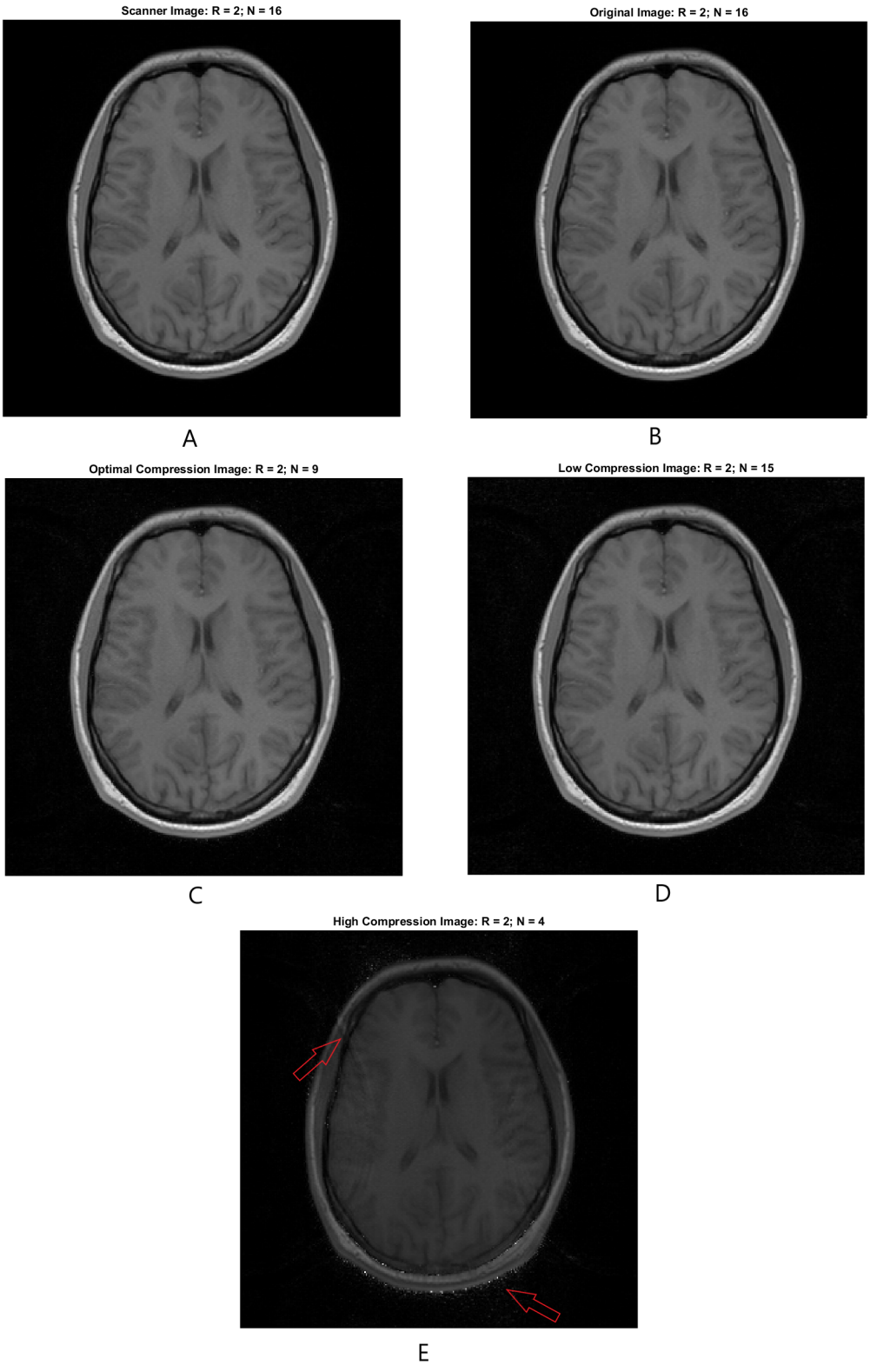

Figure 6.1: T1-weighted anatomical brain images on the transverse plane. Reference image reconstructed by Prisma scanner (A) is displayed as well as offline reconstructed images without CC (B), with optimal CC (C), low CC (D) and high CC (E). High CC enhances GRAPPA-generated overlapping artifacts, as designated with red arrows for better visibility. Furthermore, outstandingly bright voxels counterproductively affect image contrast (E).

All displayed images demonstrate a particular slice of a 2D anatomical scan. A more accurate time gain for a complete anatomical scan can be established if the single-slice time gain is multiplied by the number of slices, which is approximately 150-192 in clinical practice. Clearly, application of Coil Compression economizes time, as it is displayed both on Figure 6.3 and Figure 6.6, which serves as a justification of the motivation. Considerable time gain can be achieved, while image quality degradation is minimal, if the right set of sequence and compression parameters are applied.

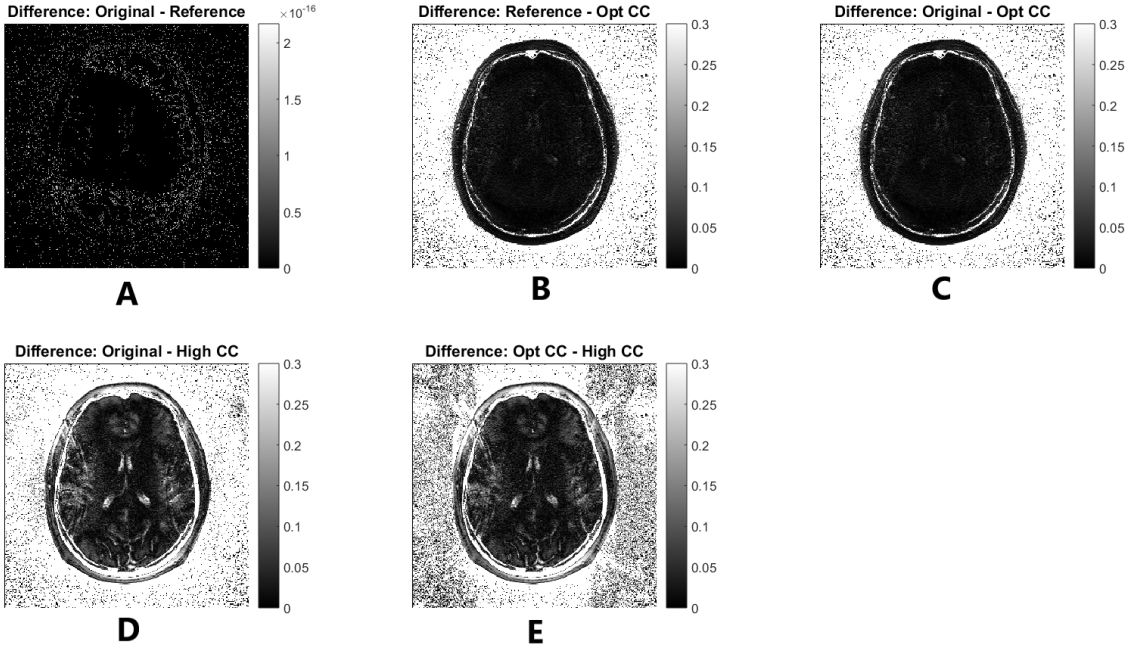

Figure 6.2: Difference images of original T1-weighted anatomical brain images on the transverse plane depicted in Figure 6.1. Difference image of Prisma reference image and original offline reconstructed image shows no deviation (A), i.e. limits on numeric data representation occur. Whereas, in consonance with stronger compression ratio, images rebuilt from highly compressed data show considerable deviation from reference image (D) and from other images gained from compressed datasets (E). The more the difference image is structured, the less the compression is efficient. Artifacts are especially distinguishable on subfigure (E), which belongs to highly compressed dataset. The wrap-around on subfigure (E) has been designated with a red arrow on subfigure (E) of Figure 6.1.

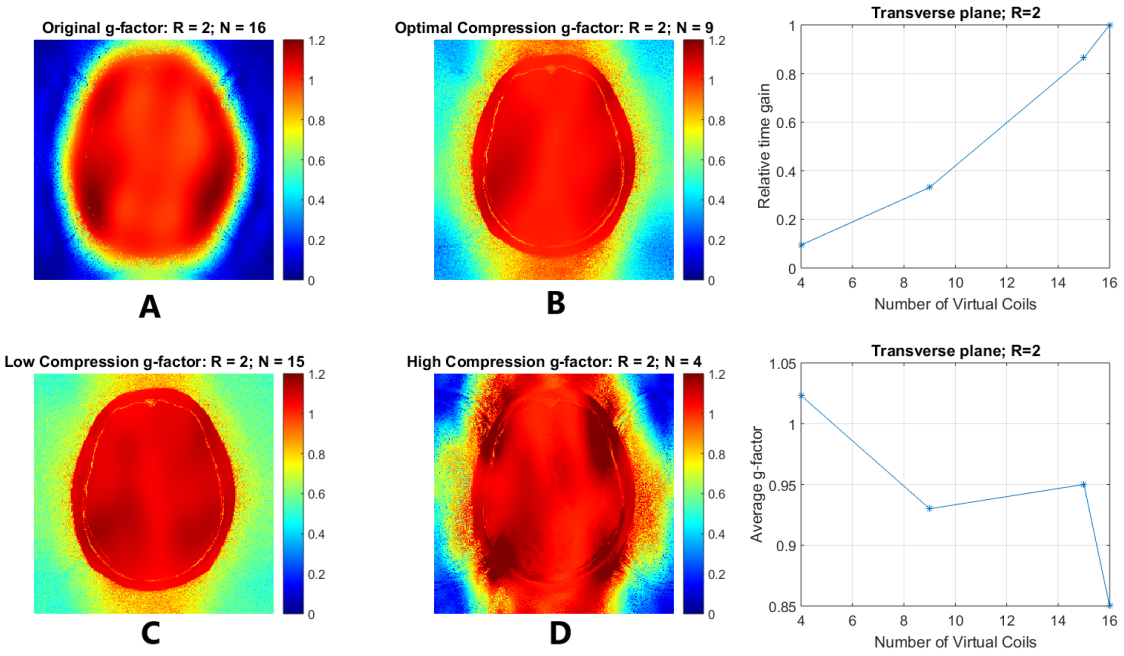

Figure 6.3: On the left: g-factors for subfigures (B), (C), (D), and (E) of Figure 6.1. Noise amplification features of high compression (D) is remarkable as well as the overlapping brain contour (D). The wrap-around on subfigure (D) has been designated with a red arrow on subfigure (E) of Figure 6.1 for better distinguishability. On the right: average g-factor and relative time gain belonging of subfigures (B), (C), (D), and (E) of Figure 6.4. It shows clearly that the more compressed the dataset is, i.e. the lower the number of virtual coils is, the higher the average g-factor is, i.e. the higher the noise amplification is.
Relative time gain plot is normalized using the reconstruction time needed for conventional GRAPPA reconstruction (N=16). GCC GRAPPA reconstruction with optimal CC (N=9) requires approximately 1/3 of the time of the conventional GRAPPA reconstruction (N=16).

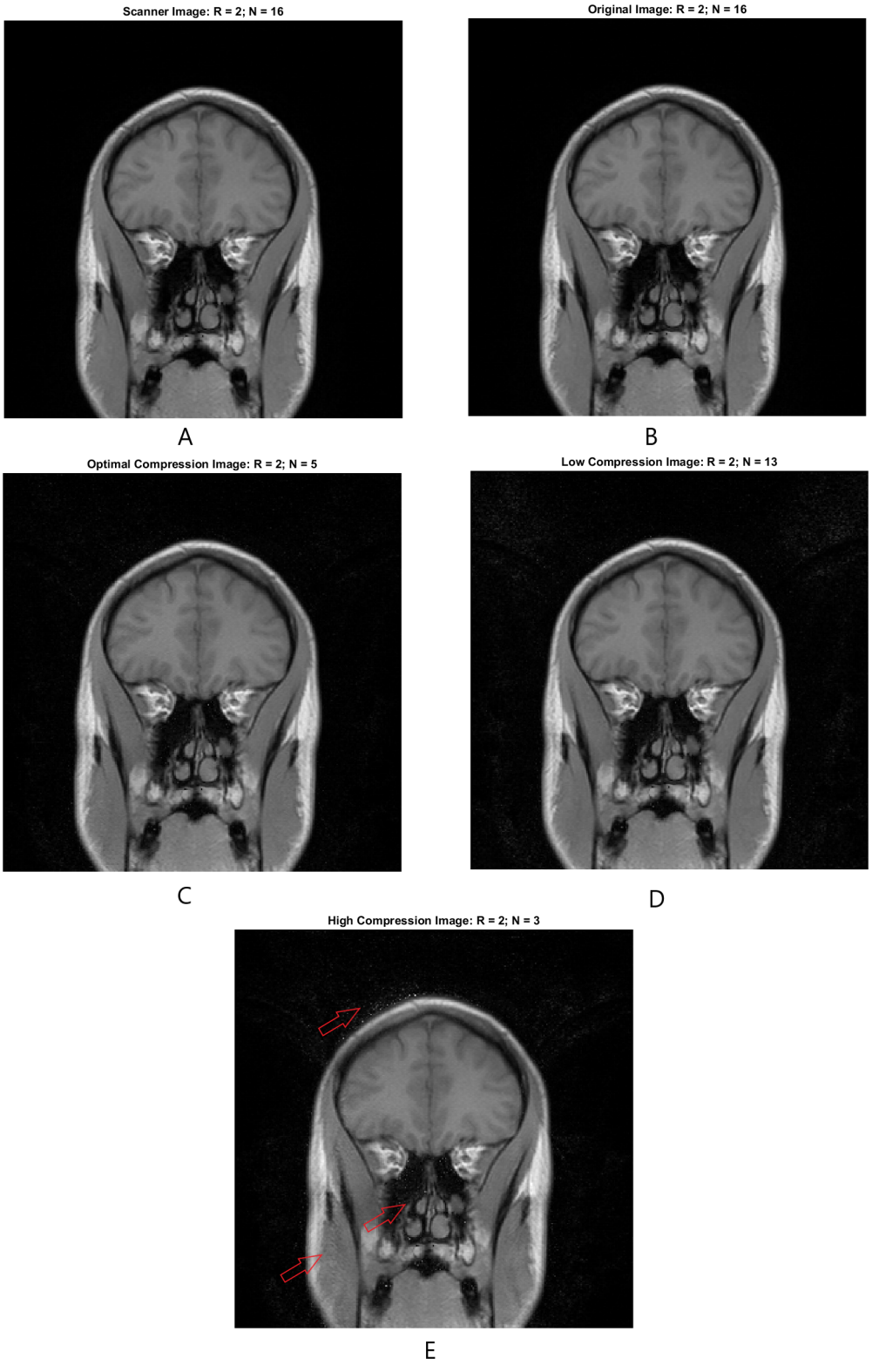

Figure 6.4: T1-weighted anatomical brain images on the coronal plane. Reference image reconstructed by Prisma scanner (A) is shown as well as offline reconstructed images without CC (B), with moderate CC (C), negligible CC (D) and considerable CC (E). Considerable CC enhances GRAPPA-generated overlapping artifacts, as designated with red arrows for better distinguishability. CC generates substantial artifacts around maxillary sinuses, more specifically at the border of the air-filled sinuses and the forming bone structure. Magnetic susceptibility changes significantly at the boundaries which is favorable for enhanced artifact occurrence.

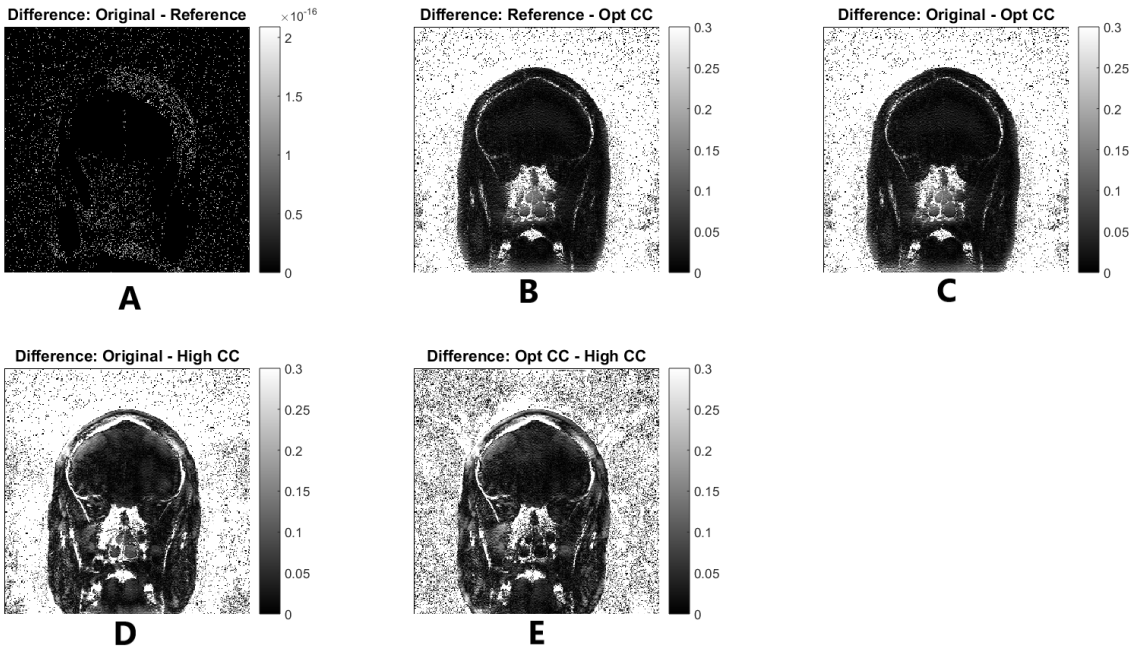

Figure 6.5: Difference images of original T1-weighted anatomical brain images on the coronal plane depicted in Figure 6.4. Difference image of Prisma reference image and original offline reconstructed image show no deviation (A), whereas, in consonance with stronger compression ratio, images rebuilt from highly compressed data (D) show considerable deviation from reference image and from other images gained from compressed datasets (E). The more the difference image is structured, the less the compression is efficient. All CC images show major noise amplification around maxillary sinuses, independently from CC ratio, which is by virtue of intense magnetic susceptibility alternation around the air-filled oral cavities.

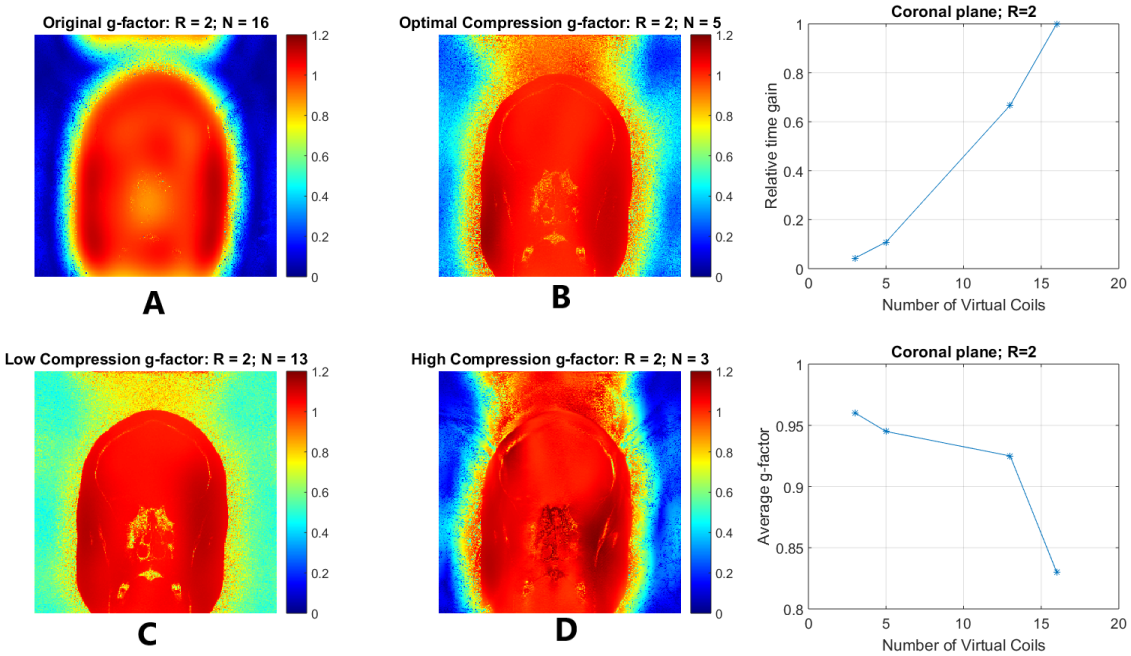

Figure 6.6: On the left: g-factors for subfigures (B), (C), (D), and (E) of Figure 6.4. Noise amplification features of high compression (D) around the maxillary sinuses are outstanding. Major artifacts have been designated with a red arrow on Figure 6.4 for better distinguishability and comparability.
On the right: average g-factor and relative time gain belonging to subfigures (B), (C), (D), and (E) of Figure 6.4. It shows clearly that the more compressed the dataset is, i.e. the lower the number of virtual coils is, the higher the average g-factor is, i.e. the higher the noise amplification is.
Relative time gain plot is normalized using the reconstruction time needed for conventional GRAPPA reconstruction (N=16). GCC GRAPPA reconstruction with optimal CC (N=5) requires approximately 1/10 of the time of the conventional GRAPPA reconstruction (N=16).

Chapter 7

Conclusion

This thesis provides a detailed theoretical overview of fundamental in-plane Parallel Imaging techniques (SENSE & GRAPPA) and of the recently introduced, respective coil compression methods (CC SENSE & CC GRAPPA). Coil compression methods offer an efficient way to overcome data redundancy on account of multiple receiver coils by compressing raw k-space data, thus drastically decreasing reconstruction time and data size sent to reconstruction hardware.

I have implemented all introduced reconstruction techniques with the respective Coil Compression methods in MATLAB environment, based on [12][13][14][15][16]. I have completed all simulations and in-vivo measurement reconstructions in MATLAB environment.

I have shown that coil compression algorithms are worth being used once an optimal set of parameters have been determined for the given measurement setup and sequence type. Time gain and the change of average g-factor by virtue of CC has been explicitly measured and coherently compared during simulations and in-vivo measurements. I have demonstrated the capacity to reconstruct in-vivo medical images from raw k-space data and to overcome compatibility issues of data extracting from a commercially available medical MRI scanner. I have reconstructed all images offline, whose quality is comparable to the image provided by the scanner. I have validated image quality using difference images and g-factor maps.

Disadvantages of CC has been shown. Higher probability of artifact occurrence due to the overuse of CC has been justified both in simulations and in-vivo measurements. Critical regions and characteristics of artifacts show correlation with daily clinical experiences [23]. Accumulated evidence indicates that my algorithms are indeed capable of reaching the same efficiency in terms of reconstruction quality as commercially available medical softwares. Determination of an optimal set of parameters for CC, depending on PI techniques and specific anatomical regions, needs further investigation. Clinical introduction would also require major contribution of radiologists.

Bibliography

[1] Griffiths, D. J., *Introduction to Quantum Mechanics*, University of Michigan, Pearson Prentice Hall, 2005.

[2] Morin, D. J., *Introduction to Classical Mechanics: With Problems and Solutions*, Cambridge, UK, Cambridge University Press, 2008.

[3] Brown, R. W., Cheng, Y.-C. N., Haacke, E. M., Thompson, M. R., & Venkatesan, R. *Magnetic Resonance Imaging: Physical Principles and Sequence Design* John Wiley & Sons Ltd, Chichester, UK, April 2014.

[4] Bloch, F., "Nuclear Induction", *Physics Review*, **70**: 460 (1946)

[5] Wang, J. , Mao, W., Qiu, M., Smith, M. B., & Constable, R. T., "Factors influencing flip angle mapping in MRI: RF pulse shape, slice-select gradients, off-resonance excitation, and B_0 inhomogeneities", *Magnetic Resonance in Medical Imaging* **56**: 463-468 (2006).

[6] Bochner, S., Chandrasekharan, K., *Fourier Transforms*, Princeton Book Comp. Publ., (2001).

[7] Carter, M., Bruce, R., "Op Amps for Everyone", Texas Instruments, (2009).

[8] Marks II, R. J., *Introduction to Shannon Sampling and Interpolation Theory*, Springer-Verlag, New York, 1991.

[9] Ferreira P. F., "Cardiovascular magnetic resonance artefacts", *Journal of Cardiovascular Magnetic Resonance* **15(1)**:41 (2013).

[10] Strang, G., "Wavelets", *American Scientist*, **82(3)**: 250–255.(May–June 1994).

[11] Demmel, J. W., *Applied Numerical Linear Algebra*, section 1.7, published by SIAM, (1997).

[12] Pruessmann, K. P.,Weiger, M., Scheidegger, M. B., & Boesiger, P., "SENSE:sensitivity encoding for fast MRI", *Magnetic Resonance in Medical Imaging* **42**: 952-962 (1999).

[13] Griswold, M. A., Jakob, P. M., Heidemann, R. M., Nittka, M., Jellus, V., Wang, J., Kiefer, B., & Haase, A. "Generalized Autocalibrating Partially Parallel Acquisitions (GRAPPA)", *Magnetic Resonance in Medicine* **47**: 1202–1210 (2002)

[14] Breuer, F. A., Kannengiesser, S. A. R., Blaimer, M., Seiberlich, N., Jakob, P. M., & Griswold, M. A., "General formulation for quantitative G-factor calculation in GRAPPA reconstructions", *Magnetic Resonance in Medicine* **62**: 739–746 (2009).

[15] Buehrer, M., Pruessmann, K. P., Boesiger, P., & Kozerke, S., "Array Compression for MRI With Large Coil Arrays" *Magnetic Resonance in Medicine* **57**: 1131–1139 (2007).

[16] Zhang, T., Pauly, J. M., Vasanawala, S. S., & Lustig, M., "Coil Compression for Accelerated Imaging with Cartesian Sampling" *Magnetic Resonance in Medicine* **69**: 571–582. (2013).

[17] Robson, P. M., Grant, A. K., Madhuranthakam, A. J., Lattanzi, R., Sodickson, D. K.. & McKenzie, Ch. A., "Comprehensive Quantification of Signal-to-Noise Ratio and g-Factor for Image-Based and k-space-Based Parallel Imaging Reconstructions" *Magnetic Resonance in Medicine* **60**: 895–907. (2008).

[18] Wang, J., Zhang, B., Zhong, K., & Zhuo, Y., "Image Domain Based Fast GRAPPA Reconstruction and relative SNR degradation Factor", . In: Proc 13th Annual Meeting ISMRM, Miami; 2005:2428.

[19] Penrose R., "A generalized inverse for matrices", *Mathematical Proceeding of the Cambridge Philosophical Society* **52(3)**: 403-416 (1995).

[20] Jolliffe I., *Principal Component Analysis* In: Lovric M. (eds) International Encyclopedia of Statistical Science, Springer, Berlin, Heidelberg (2011).

[21] Golub, G.H., Reinsch, C., *Singular Value Decomposition and Least Squares Solutions*, In: Bauer F.L. (eds) Linear Algebra. Handbook for Automatic Computation, vol 2. Springer, Berlin, Heidelberg, (1971).

[22] de Zwart, J. A., Ledden, P. J., Kellman, P., van Gelderen P.,& Duyn, J. H., "Design of a SENSE-optimized high-sensitivity MRI receive coil for brain imaging" *Magnetic Resonance in Medicine* **47**: 1218–1227 (2002).

[23] Wippold II MD,F. J., "Head and neck imaging: The role of CT and MRI", *Journal of Magnetic Resonance Imaging*, **25(3)**: 453-465 (2007).

[24] Clerk Maxwell, J., "A treatise on electricity and magnetism", Vol. II. Oxford: Clarendon Press. ch. III, sec. 530, p. 178. (1881).

[25] Hazewinkel, M., "Stokes formula", Encyclopedia of Mathematics, Springer Science+Business Media B.V. / Kluwer Academic Publishers, ed. (2001) [1994].

[26] Jackson, J., "Classical electrodynamics", Wiley, New York, NY, 3rd ed. edition, (1999).